Characterisation of HV-CMOS silicon pixel sensors with a transient current technique before and after proton irradiation

Master Thesis
at the Faculty of Science
University of Bern

submitted by
Armin Fehr

March 2018

Supervisor:
Prof. Dr. Michele Weber

Albert Einstein Center for Fundamental Physics
Laboratory for High Energy Physics

Abstract

For operation at the High Luminosity LHC, the ATLAS detector will need to be upgraded. Its Inner Detector will be replaced by an all-silicon tracking system called the Inner Tracker (ITk). The ITk will cope with harsher radiation conditions and a higher number of simultaneous collisions with respect to the current LHC environment. The ATLAS Collaboration is currently developing a new monolithic radiation hard sensor for the outer ITk pixel detector layers. This new sensor technology is based on the High Voltage CMOS (HV-CMOS) process, which makes the integration of CMOS electronics on a high voltage biased substrate possible. This enables such sensors to operate in a high radiation environment, the material budget can be reduced and the production can be simplified. A study of the radiation hardness of prototype HV-CMOS sensors is presented in this thesis. In particular, a characterisation of the depletion depth with the transient current technique was performed. To calculate the depletion depth, a dedicated analysis was developed. The study covers the performance before and after proton irradiation with fluences up to $1.5 \cdot 10^{15}$ 1 MeV $\mathrm{n_{eq}/cm^2}$. Two proton beams with different energies were exploited for the study. The irradiation with protons of 24 GeV was performed at CERN's Proton Synchrotron, while an irradiation with 16.7 MeV protons was conducted at the Bern Cyclotron. For the latter, an irradiation setup measuring the proton flux was developed. The acceptor removal seen in neutron irradiation of HV-CMOS sensors is also observed in the proton irradiations, but to a much larger extent. This increases the depletion depth after proton irradiation to more than 100 µm.

Acknowledgements

I want to thank the people from the Bern ATLAS group for sharing their knowledge. Special thanks goes to Antonello Miucci who has always supported me during lab work and in the writing process. Furthermore I am grateful for the encouraging words of my friends and family, especially of my girlfriend Susanne Ilg, who always believed in me.

Contents

Introduction

Curiosity about nature has led humankind to many impressive discoveries, improving our understanding of its guiding principles. Particle physics seeks to grasp the fundamental objects of nature and their interactions. The Standard Model of particle physics provides a unified description of the strong, electromagnetic and weak interactions in terms of gauge theories. The Standard Model describes processes along many orders of magnitude to a remarkable precision. It predicted many particles such as the Higgs Boson discovered in 2012 [1], but still leaves crucial questions unanswered.

The most fundamental shortcomings of the Standard Model are that it neither includes gravity nor accounts for dark matter and dark energy, which are predicted by cosmology. There are several theories trying to overcome the limitations of the Standard Model such as theories of Supersymmetry. Together with other theories, they predict new fundamental particles at high energies at the order of tera electron-volt (TeV).

Such particles can either be searched for directly or indirectly. In the first case the particles are produced by high energy collisions at particle accelerators, if the centre of mass energy is higher than their mass. For example, many Supersymmetry scenarios contain squarks with quite high masses, leading to a low predicted cross section. Since a large number of events are needed to claim discovery, many collisions must be generated to confirm the existence of such a new particle. The number of collisions created in a particle physics experiment is proportional to the integrated luminosity $L_{\text{int}} = \int \mathcal{L}\, \mathrm{d}t$ with $\mathcal{L}$ being the (instantaneous) luminosity. Consequentially the two main requirements for discovering new particles are high energy and high luminosity, as both increase the discovery potential of the machine.

The LHC will be upgraded to deliver a higher instantaneous luminosity in 2025-2026 in the framework of the High Luminosity LHC program (HL-LHC). With this increase in luminosity, the number of simultaneous collisions (pile-up) increases and the detectors receive more radiation damage. The experiments at the LHC will therefore also need to be upgraded in order to cope with the challenges posed by HL-LHC.

High voltage complementary metal-oxide-semiconductor (HV-CMOS) sensors are possible candidates for pixel layers of the Inner Tracker (ITk) of the ATLAS (**A** **T**oroidal **L**HC **A**pparatu**S**) detector at HL-LHC, since they are radiation tolerant and allow to reduce the material budget. This is particularly true for the outer layers where many sensors are needed.

In this work, the depletion depth of the H35 demonstrator chip produced in the HV-CMOS technology is measured for fluences of up to $1.5 \cdot 10^{15}$ 1 MeV neutron equivalent

fluence per square centimetre. This characterisation is performed using the Transient Current Technique (TCT). The TCT setup is validated and a dedicated analysis is developed to calculate the depletion depth. Sensors of different resistivities are irradiated with 16.7 MeV protons at the Bern Cyclotron, for which an irradiation setup is developed. A second proton irradiation is performed at the CERN Proton Synchrotron (PS) with 24 GeV protons. The evolution of the depletion depth under the two proton irradiations is then compared with results from neutron irradiation of the same chip.
Chapter 1 describes the guiding principles of particle physics experiments and presents the Large Hadron Collider and the ATLAS detector, continuing with the description of the ITk. In Chapter 2, the working principles of silicon pixel detectors, and how they are affected by radiation damage, are explained. Furthermore, the HV-CMOS technology is introduced. The TCT used for the characterisation of the sensors is presented in Chapter 3, together with the results of the technique on non-irradiated samples. Chapter 4 guides through the irradiation campaign at the Bern Cyclotron and presents the TCT results of the irradiated samples. The differences between the irradiation campaigns are also discussed. Finally, conclusions are drawn and an outlook on future studies is presented.

Chapter 1

The Large Hadron Collider and the ATLAS experiment

This chapter introduces the key concepts for high energy particle physics experiments, beginning with some basic accelerator design principles. Next, an overview of the LHC and the ATLAS detector is presented. Finally, the chapter concludes with the description of the high luminosity program at the LHC and the replacement of the Inner Detector of ATLAS by the ITk.

1.1 Accelerator design principles

Charged particles can be accelerated using radio frequency (RF) cavities. The beam of particles can then either hit a solid target (*fixed-target experiments*) or be brought into a collision with another beam of particles (*collider experiments*). The centre of mass energy of an experiment is equal to the square root of the Mandelstam variable s, which is defined as

$$s = (E_1 + E_2)^2 - (\vec{p}_1 + \vec{p}_2)^2 \tag{1.1}$$

with $\vec{p}_{1,2}$ the momenta of the colliding particles and $E_{1,2}$ their energy. For a fixed-target experiment $\sqrt{s} = \sqrt{m_1^2 + m_2^2 + 2m_2E_1}$, this results in an centre of mass energy of 114.6 GeV for a 7 TeV proton beam hitting a hydrogen target. Colliding two such proton beams leads to $\sqrt{s} = 2E = 14\,\text{TeV}$ [2], which is the design energy of the LHC. Since the centre of mass energy is much higher in the collider case, such a design is adopted for particle physics accelerators seeking high energy collisions.
Because the energy gained in RF cavities is smaller than 100 MeV/m (as e.g. in CLIC [3]), the particles have to pass through many cavities in order to reach TeV energies. This can either be achieved by building a long straight linear accelerator with many RF cavities placed one after each other, or a circular accelerator where the particles pass a small number of RF cavities many times. In the latter case, magnets are used to guide the

particles along a circular path. The Lorentz force has to counteract the centripetal force:

$$q\left|\vec{E}+\vec{v}\times\vec{B}\right| = \frac{E}{r}\,. \tag{1.2}$$

q, E and $\vec{v}$ are the charge, energy and velocity of the particle, while r is the radius of the circular accelerator. $\vec{E}$ and $\vec{B}$ are the electric and magnetic fields generated by the magnets. Neglecting $\vec{E}$, setting $v = c = 1$ and having $\vec{B}$ perpendicular to $\vec{v}$, Equation (1.2) becomes

$$E = q|\vec{B}|r\,. \tag{1.3}$$

For a fixed r, $|\vec{B}|$ needs to grow synchronously with the energy. This is why circular accelerators with a fixed radius are called *synchrotrons*. To allow the particles to reach high energies, the magnetic field strength and the radius of the synchrotron must be large. Since charged particles undergo synchrotron radiation when forced into a circular orbit they constantly lose energy. This energy loss is proportional to $1/m^4$. At TeV energies protons lose almost no energy, while the much lighter electrons have a high energy loss. Due to this, protons can reach much higher energies in a circular accelerator.

1.2 The Large Hadron Collider

With the above mentioned requirements in mind, the Large Hadron Collider (LHC) [4] was designed for an unprecedented high centre of mass energy of $\sqrt{s} = 14\,\text{TeV}$ (currently 13 TeV) and a design luminosity of $10^{34}\,\text{cm}^{-2}\,\text{s}^{-1}$, already exceeded as for example seen in the peak luminosity of $2.2 \times 10^{34}\,\text{cm}^{-2}\,\text{s}^{-1}$ in 2017 [5].
The LHC is a synchrotron hadron collider with a circumference of 26.7 km at the European Organization for Nuclear Research (CERN) in Geneva, Switzerland. It replaced the Large Electron-Positron Collider [6]. The design energy of the LHC is more than one order of magnitude higher than the previous largest accelerator Tevatron at FermiLab [7]. The LHC is used for proton-proton, lead-lead and proton-lead collisions, of which only proton-proton collisions are discussed in this chapter.
The LHC is the last element of a chain of pre-accelerators as seen in Figure 1.1. Initially, hydrogen gas is stripped off its electrons. The produced protons are accelerated by the linear accelerator Linac 2 to 50 MeV, injecting the beam into the Proton Synchrotron Booster (BOOSTER). In the following stages, synchrotrons are used to gradually increase the beam energy. In each revolution, the energy is increased slightly until the extraction beam energy is reached and the beam is guided to the next acceleration stage. The protons are accelerated until they reach an energy of 1.4 GeV. The Proton Synchrotron (PS) then increases the beam energy to 25 GeV and forms the bunch structure. The last pre-accelerator, the Super Proton Synchrotron (SPS), accelerates the beam to 450 GeV. The bunches of protons in the SPS are then injected into the two beam pipes of the LHC, in which the bunches travel in opposite directions and are accelerated to their final energy.

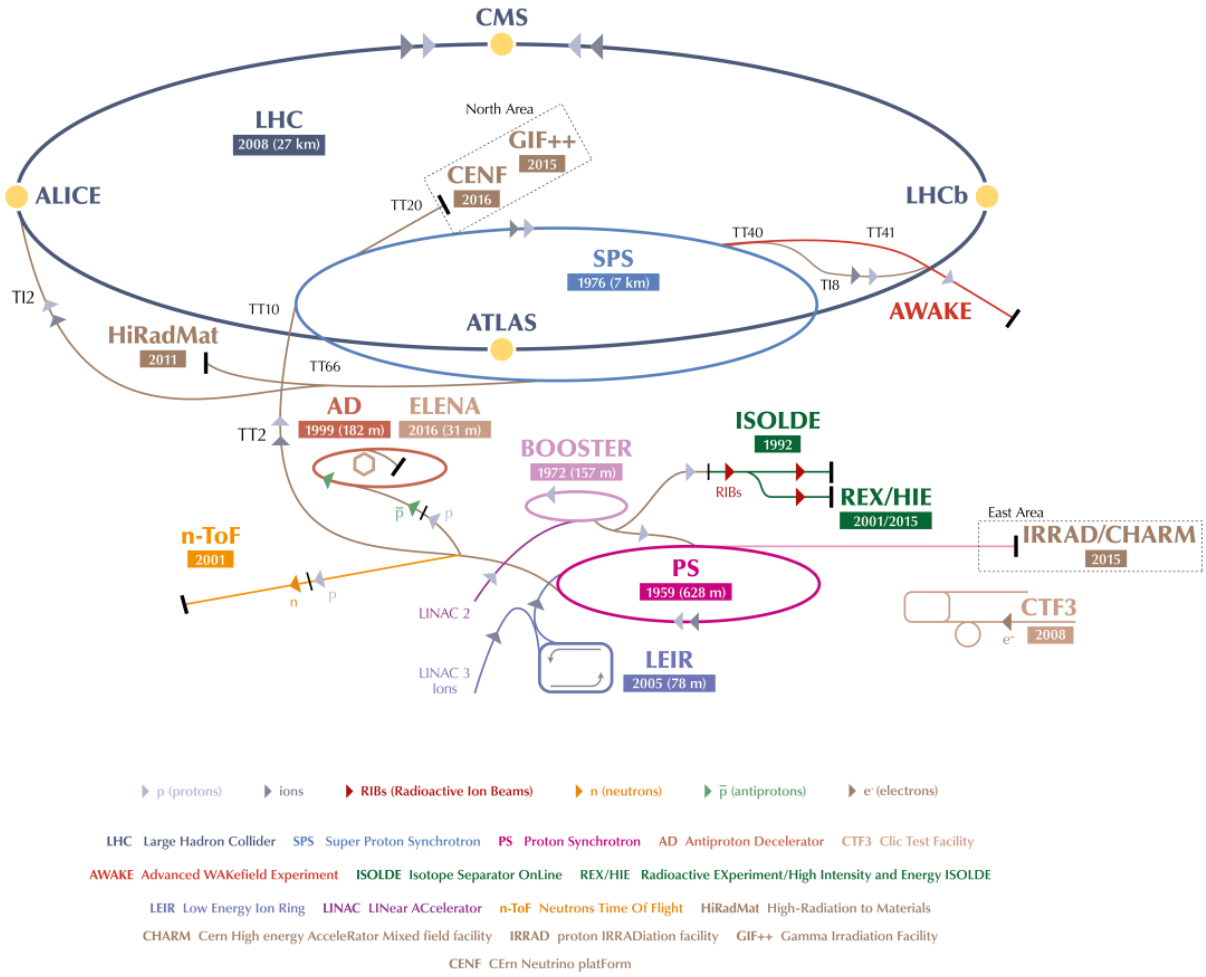

Figure 1.1: The CERN accelerator complex taken from [8]. The protons are first accelerated by Linac 2, to then go into the first circular accelerator, the Proton Synchrotron Booster (BOOSTER). The next stages of acceleration are the Proton Synchrotron (PS), where the bunch structure is formed, and the Super Proton Synchrotron (SPS). From there, the two beam pipes of the LHC are filled with bunches. When the protons reach their final energy, the two beams are brought into collision at the four interaction points, where the four big experiments ATLAS, CMS, LHCb and ALICE are recording the collisions.

The beam pipes are embedded in a magnet structure consisting of one dipole magnet per beam pipe. The resulting magnetic field points in opposite directions for the two beam pipes. As discussed in Section 1.1, the resulting Lorentz force on the protons keeps them on a circular path. Higher order magnets are used for shaping the bunches and focusing the beams. When fully filled, the LHC can host up to 2808 bunches with $\sim 10^{11}$ protons each. The bunch spacing is 25 ns, which corresponds to a collision rate of 40 MHz. By changing the quadrupole settings, the orbits of the two beams are adjusted to bring them into collision at the interaction points. For each bunch crossing, multiple proton-proton collisions happen *pile-up*, each having many partons interacting.
At the interaction points, the four big experiments ATLAS, CMS, LHCb and ALICE are located and record the collisions. Since this thesis characterises candidate sensors for the high luminosity upgrade of the ATLAS detector, the following section presents the current layout of ATLAS.

1.3 The ATLAS Detector

ATLAS [9] is a general purpose detector. Its schematics and dimensions are shown in Figure 1.2. ATLAS covers almost the whole solid angle, with the exception of the area close to the beam pipe. It features a cylindrical geometry and has a barrel part close to the interaction point and end-caps adjacent to the ends of the barrel. ATLAS consists of numerous sub-detectors, each responsible for the detection of some of the various particle signatures.
Directly outside of the beam pipe is the Inner Detector (ID). In order to cope with the aforementioned pile-up, the interaction point and primary and secondary vertices need to be accurately and quickly located and matched together. This procedure is called *tracking*. The trajectories of charged particles are bent under the 2 T magnetic field of the solenoid magnet. Measuring the curvature of a particle track, its momentum and charge can be inferred. The ID features the Pixel Detector consisting of four silicon pixel layers with the innermost being the Insertable B-Layer [11]. Next comes the Semiconductor Tracker. The outermost piece of the ID is the Transient Radiation Tracker.
The next sub-detector is the calorimetry system consisting of the electromagnetic (ECAL) and hadronic (HCAL) calorimeters. Electrons and photons lead to electromagnetic showers measured in the ECAL, while hadronic showers are produced by hadrons in the HCAL.
The outermost sub-detector is the muon spectrometer. The toroidal magnet system creates a magnetic field that bends the muons. Muon trackers measure these trajectories, inferring the momenta of the muons.
The following section discusses the replacement of the ID by the Inner Tracker in the framework of the High-Luminosity LHC (HL-LHC) program.

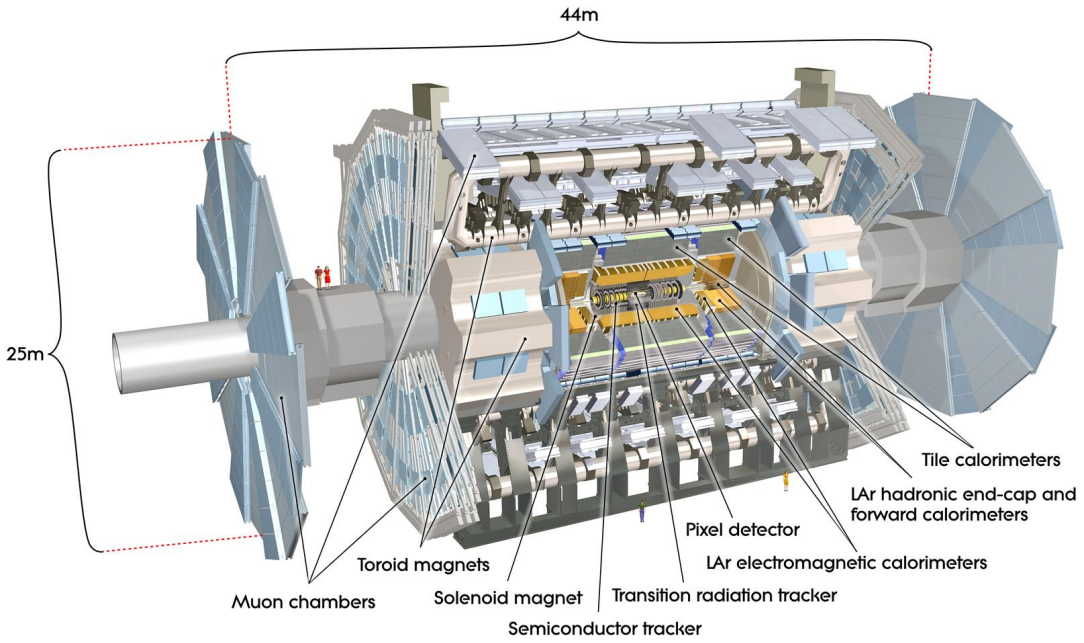

Figure 1.2: Current layout of the ATLAS detector taken from [10]. Closest to the beam pipe around the interaction point is the Inner Detector consisting of the Pixel Detector, the Semiconductor Tracker and the Transition Radiation Tracker. Next comes the solenoid magnet, followed by the Liquid Argon (LAr) Calorimeter. It contains LAr electromagnetic calorimeters, as well as LAr hadronic end-cap and forward calorimeters. The other part of the calorimeter system is the Tile Calorimeter in the barrel region. The farthest away from the interaction point is the Muon Spectrometer consisting of muon chambers and the characteristic toroid magnet system.

1.4 High luminosity program and Inner Tracker

The timeline of the LHC and the HL-LHC programs are seen in Figure 1.3. The LHC will be upgraded in the long shutdown 3 (LHS3) in 2024-2026 to deliver higher luminosity to the experiments. The LHC will reach a peak instantaneous luminosity of $\mathcal{L} = 7.5 \times 10^{34}\,\mathrm{cm}^{-2}\,\mathrm{s}^{-1}$ after the upgrade. For the whole lifetime of the LHC, this is equivalent to an integrated luminosity of between 3000 and 4000 fb^{-1}.

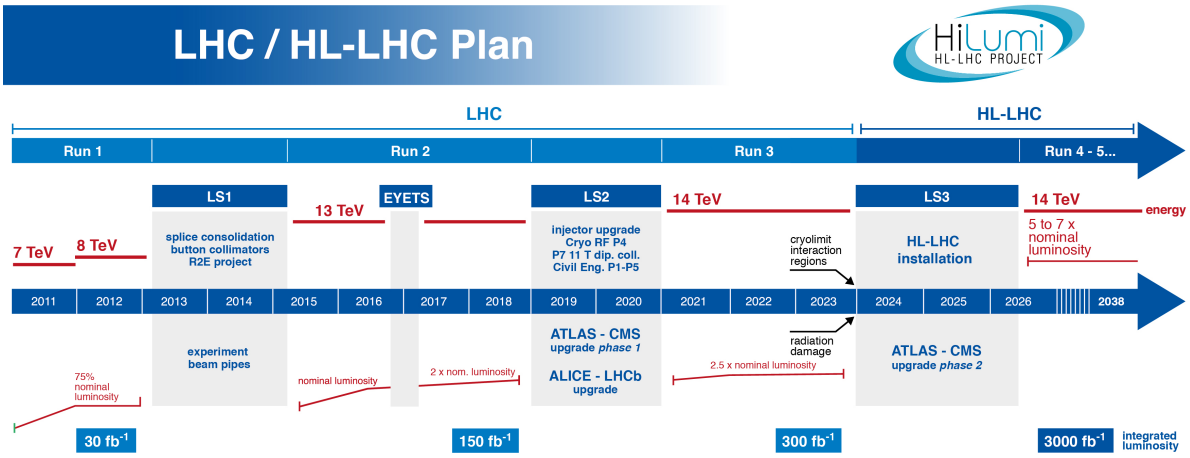

Figure 1.3: Timeline of the LHC and High Luminosity LHC programs taken from [12]. The HL-LHC will be installed in 2024-2026. At the same time, ATLAS and CMS receive their phase 2 upgrade. HL-LHC will then run at a instantaneous luminosity 5–7 times higher than the nominal luminosity for more than ten years, reaching an integrated luminosity of $\sim 3000\,\mathrm{fb}^{-1}$.

This larger number of collisions is accompanied by an expected pile-up of ~ 200 [13] in the detectors, which is much higher than ~ 40 in 2017. In order to distinguish all tracks and ensure track and vertex reconstruction capabilities with this high number of pile-up events, new high granularity detectors are needed. Such systems must also withstand the harsher radiation environment due to the higher luminosity.
At the time of HL-LHC installation, ATLAS and CMS will implement their phase 2 upgrades. Among other improvements, the ATLAS ID will be replaced by the Inner Tracker (ITk), an all-silicon detector to cope with the challenges posed by high luminosity. ITk consists of an inner silicon pixel and an outer silicon strip detector as described in the corresponding Technical Design Reports [13, 14]. The pixel detector hosts five layers of sensors arranged in the *Inclined Duals* layout (baseline design) seen in Figure 1.4. The most prominent features are the barrel stave, which is prolonged with a section hosting inclined modules, and the end-cap ring system. The total silicon area of the pixel detector is $\sim 20\,\mathrm{m}^2$, which is around 10 times larger than the current detector installed in ATLAS. Radiation damage is expressed in a fluence (particles/cm^2) of 1 MeV neutrons, that would have inflicted the same radiation damage (1 MeV neutron equivalent fluence $\mathrm{n_{eq}}$, see

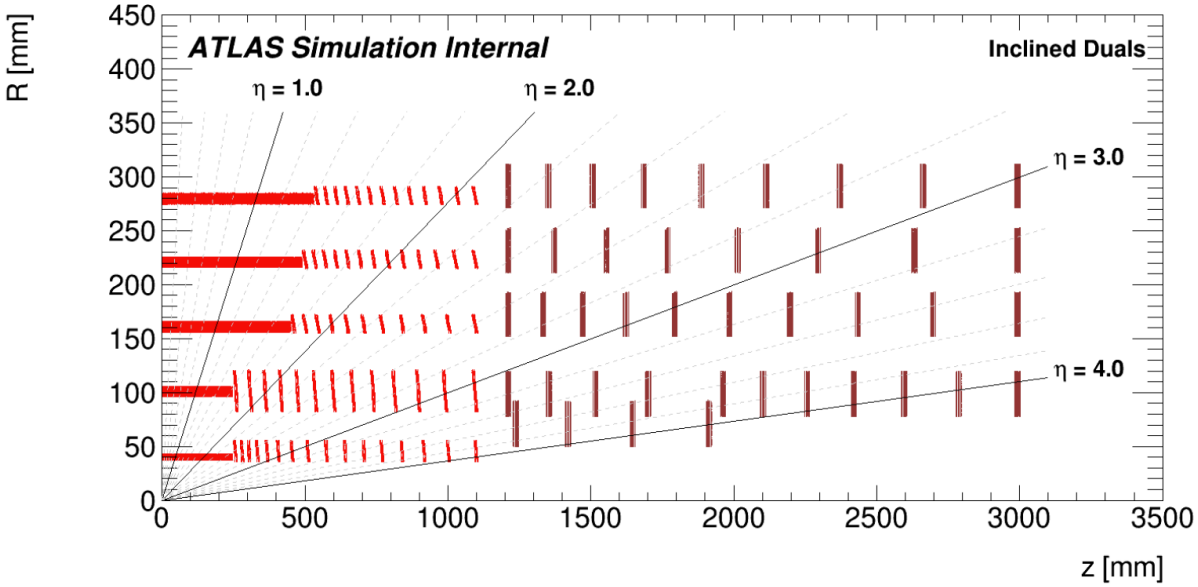

Figure 1.4: ATLAS ITk Inclined Duals Pixel layout taken from [13]. Only one quadrant and only active detector elements are shown. z is along the beam line with zero being the interaction point. R is the radius measured from the interaction point. The barrel (red) lying close to the interaction point is prolonged with a section of inclined modules. At $|z| > 1100\,\text{mm}$, the end-cap ring system (dark red) is placed.

Section 2.4). Figure 1.5 shows the cumulative radiation damage in the pixel detector of the ITk over the lifetime of HL-LHC in 1 MeV $\text{n}_{\text{eq}}/\text{cm}^2$ fluence. The closer the detector is to the beam pipe, the higher the received radiation. The ITk innermost layers will be populated by *hybrid* detectors, in which silicon sensors are bump-bonded to front-end chips. Hybrid detectors are used as they are the most radiation tolerant solution at the moment, but their production cost is high mostly due to bump-bonding. For the outer layers, where the requirements of radiation hardness can be relaxed, the more economical use of High Voltage CMOS (HV-CMOS) sensors is considered [15] and will be discussed in Section 2.5. The red box in Figure 1.5 marks the outermost (fifth) pixel layer, in which the fluence goes up to $\sim 10^{15}$ 1 MeV $\text{n}_{\text{eq}}/\text{cm}^2$.
In the following chapter, the interaction of particles with silicon is discussed, to then explain the working principle of silicon semiconductor sensors. This is followed by a discussion of radiation damage in silicon. Lastly, the monolithic technology and HV-CMOS sensors are discussed.

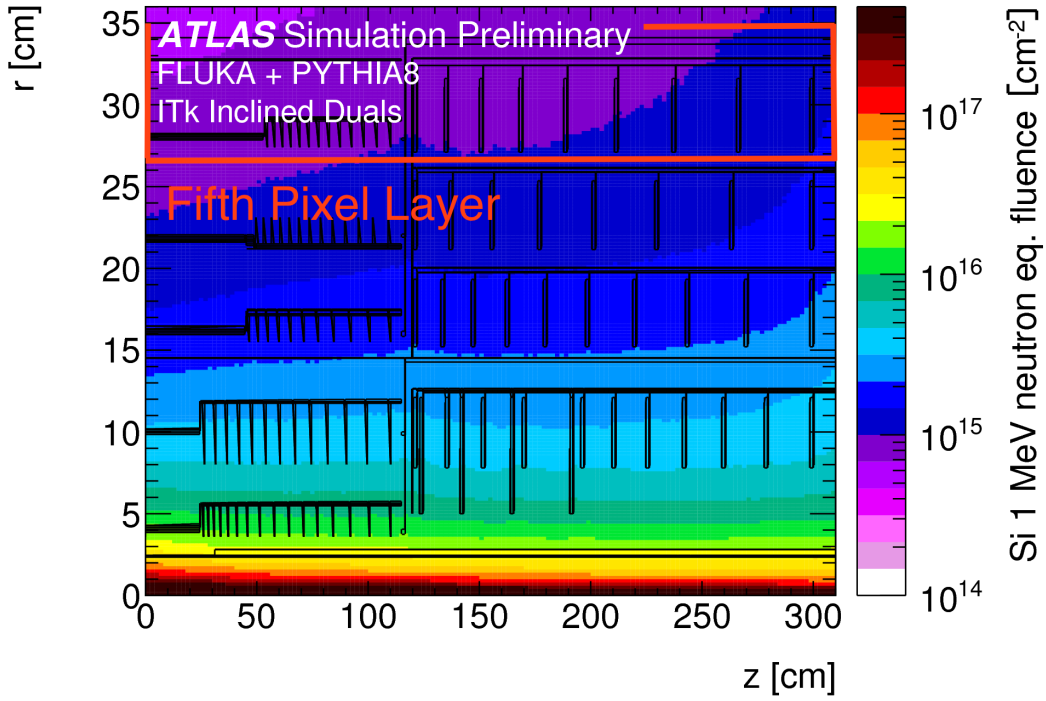

Figure 1.5: Fluence distribution in 1 MeV neutron equivalent fluence per centimetre square in the ITk Inclined Duals design taken from [13]. The distribution is calculated by a FLUKA [16] and PYTHIA8 [17] simulation. Marked in red is the fifth pixel layer, for which sensors produced in the HV-CMOS technology are considered. The fluence in this region is $\sim 10^{15}$ 1 MeV n_{eq}/cm^2.

Chapter 2

Silicon pixel detectors

Silicon pixel detectors are the main detectors of precision tracking systems in high energy particle physics. This chapter gives a short overview about the detection of particles with silicon detectors as well as how the sensors are affected by radiation damage. One of the main ongoing developments for silicon detectors is to combine the sensor and the data digitisation in a single chip, referred to a *monolithic design*. Such a chip is enabled by the High-Voltage CMOS technology. Sensors developed in this framework are investigated for use in the outer layers of the ITk. Prototype chips of the 350 nm HV-CMOS technology have been investigated in this thesis.

2.1 Particle interaction with silicon

The particle interaction with matter depends on the particle's nature and the characteristics of the target material. The main interactions are ionisation for charged particles, nuclear interactions for hadrons and electromagnetic interactions for photons.
A charged particle passing through a layer of material can ionise it, due to which the particle loses part of its energy. The energy lost by ionisation in the material generates an electric signal so that this phenomenon can be used to detect charged particles. The Bethe-Bloch formula [18, 19] describes the mean energy loss per unit length due to ionisation. It is valid for relativistic particles ($0.05 < \beta\gamma < 500$ [20]) with masses $m >> m_\mathrm{e}$ (the mass of an electron) and follows:

$$-\left\langle \frac{\mathrm{d}E}{\mathrm{d}x} \right\rangle_{\mathrm{Ion.}} = \frac{4\pi r_\mathrm{e}^2 m_\mathrm{e} c^2 N_\mathrm{A} Z z^2 \rho}{A\beta^2} \left\{ \frac{1}{2} \ln \left(\frac{2m_\mathrm{e}c^2\beta^2\gamma^2 T_\mathrm{max}}{I^2} - \beta^2 - \frac{\delta(\beta\gamma)}{2} \right) - \frac{C}{Z} \right\} \quad (2.1)$$

r_e is the classical radius of the electron, $\beta = v/c$ the speed of the particle relative to the speed of light c and $\gamma = 1/\sqrt{1-\beta^2}$ is the Lorentz factor. N_A is the Avogadro constant, Z and A are the atomic and mass number of the material, ρ is the density of the material and z is the particle's charge in units of the electron charge e. I is the mean excitation energy of the material (depending on Z). The empirical formula for the mean excitation energy is $I = I_0(Z) \cdot Z + I_1(Z)$, which leads to $I = 170.8\,\mathrm{eV}$ for silicon. T_max is the

maximal energy transferred to a free electron in a single collision. Lastly, C and δ are the shell and density corrections.
Figure 2.1 shows the energy loss per unit length and density due to ionisation calculated with Equation (2.1) of different particles for several elements. Once the particle and material are fixed, the energy loss only depends on $\beta\gamma$. The minimal energy loss for all materials is at $\beta\gamma \sim 3$–4 for particles with charge one. A particle with such an energy loss is called a *minimum ionising particle* (MIP). For $\beta\gamma > 500$, the Bethe-Bloch formula is not valid anymore since radiative effects become dominant [20].

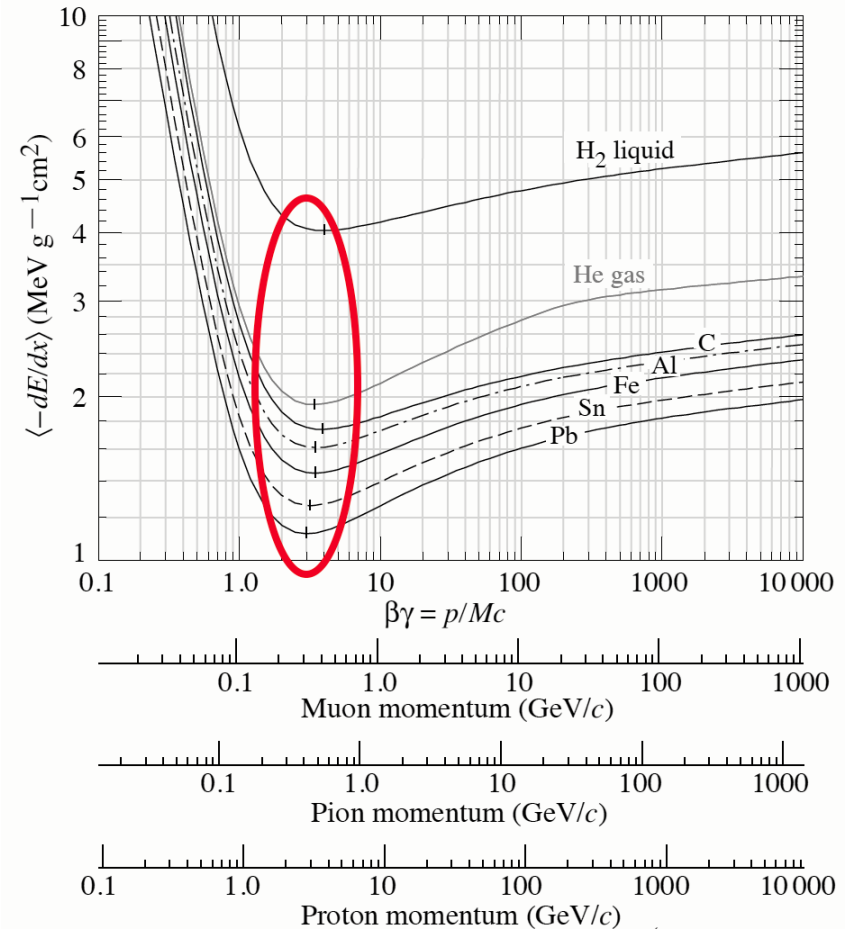

Figure 2.1: The energy loss per unit length and density by ionisation calculated with the Bethe-Bloch formula (Equation (2.1)) for different materials and a particle with electric charge ± 1 taken from [21]. The formula is valid for particles with $0.05 < \beta\gamma < 500$ and masses $m \gg m_e$. The energy loss in silicon is similar to aluminium. The minimal energy loss is at $\beta\gamma \sim 3$–4 as marked in red.

The energy loss depends on the thickness of the absorber material. As an example, Figure 2.2 shows the energy loss distribution of 500 MeV pions for silicon of different thicknesses. The Landau-Vavilov function [22, 23] (or straggling function) describes the energy loss probability distribution in thin absorbers. This is true if the mean energy

loss in a material of a given thickness $\bar{\Delta}$ is small compared to the maximum possible energy transfer $W_{\max}$ ($\kappa = \bar{\Delta}/W_{\max} \leq 0.05$–$0.1$ [24]). For thick absorbers ($\kappa > 10$) the distribution approaches a Gaussian [24].

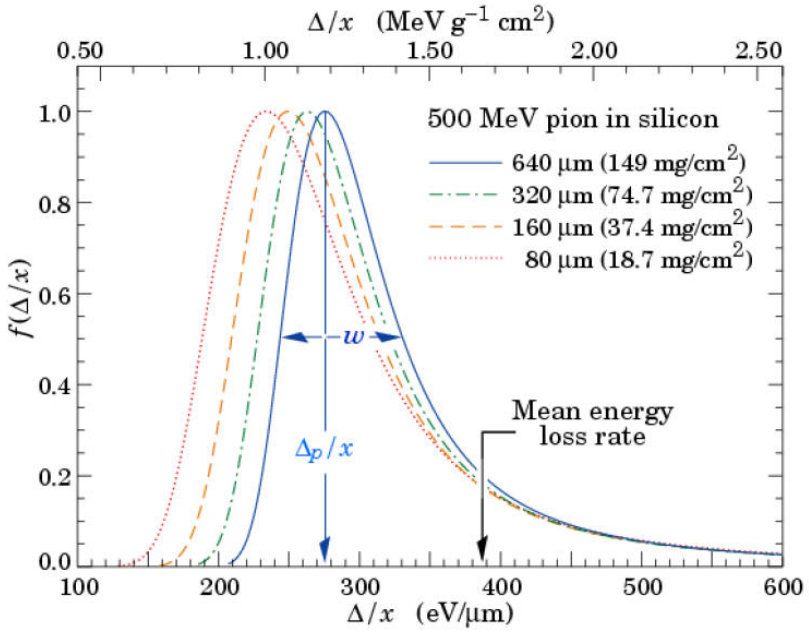

Figure 2.2: Energy loss distribution of 500 MeV pions in silicon of different thicknesses, normalised to one at the most probable energy loss taken from [24]. w is the full width half maximum (FWHM). The distribution approaches a Gaussian for increasing thicknesses.

The amount of ionisation a material has taken is expressed as the *total ionising dose* (TID) defined as

$$\mathrm{TID} = \frac{1}{\rho}\left(\frac{\mathrm{d}E}{\mathrm{d}x}\right)_{\mathrm{Ion.}} \cdot \Phi_{\mathrm{part}} \tag{2.2}$$

with Φ_{part} being the particle fluence.
The electromagnetic interaction of photons with matter is described by three processes: The photoelectric effect, the Compton effect and pair production as seen in Figure 2.3. The photoelectric effect is dominant at $E \lesssim 0.05\,\mathrm{MeV}$ and has a Z^4–Z^5 dependency [25]. The Compton effect is linearly proportional to Z and takes over up to energies of $\sim 10\,\mathrm{MeV}$ [26]. Finally, the pair production is dominant for higher energies, featuring a Z^2 proportionality [26].
At low energy the photon cross-section with silicon is high enough so that it can be used as a detection material with reasonable efficiency. For example, silicon is exploited in photomultipliers or CMOS imaging sensors. In the TCT, described in Chapter 3, infrared photons are used to characterise silicon sensors taking advantage of the photoelectric effect.
Hadrons can interact with matter by nuclear interactions, which are the dominant pro-

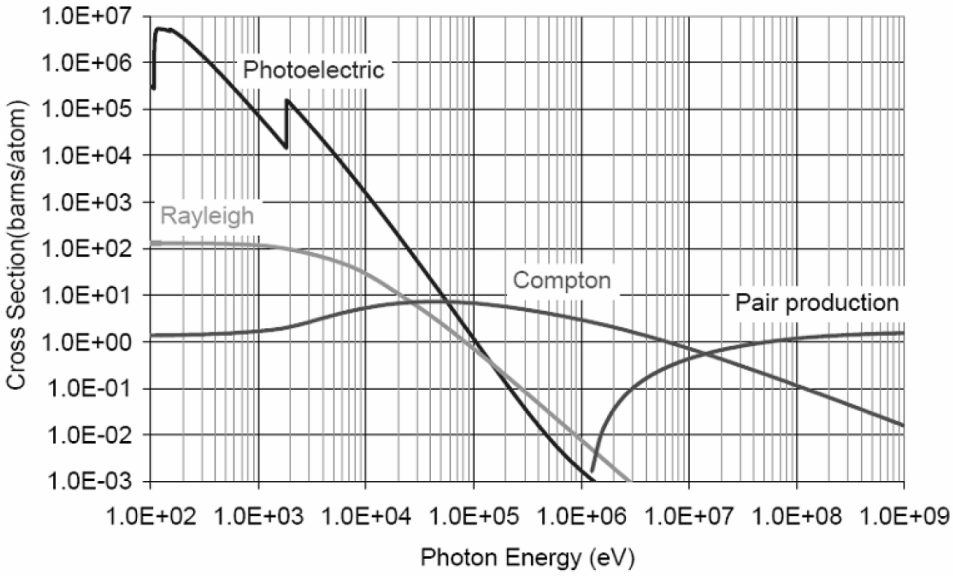

Figure 2.3: Cross sections of the various photon interactions in silicon taken from [27]. At low energies $E \lesssim 0.05\,\text{MeV}$, the photoelectric effect is dominant. The Compton effect takes over until energies of $\sim 10\,\text{MeV}$. Finally, pair production is dominant for higher energies.

cesses in case of neutrons. Charged hadrons also ionise the material as discussed above. At low energies (eV-keV), neutrons mostly interact with matter by neutron capture, but other nuclear reactions are possible. Up to $\sim 1\,\text{MeV}$, inelastic scattering can happen. In this process, the nucleus gets excited by the neutron and then decays, emitting a neutron and a photon. In the MeV region, the elastic nuclear scattering is dominant. The lighter the nuclei, the more energy the impinging neutron loses. For high energy neutrons with $E \geq 100\,\text{MeV}$, the neutron produces hadronic showers. [20]

2.2 Semiconductors and p-n junction

In semiconductors, atoms share some or all of their valence electrons with their neighbour atoms. This forms covalent bonds. The dynamic description of this phenomenon is given by the band theory, where the energy levels of different atoms collapse in band levels because of the Pauli exclusion principle. In particular, the energy levels of valence electrons create the valence band, while the possible energy levels for excited atoms degenerate into the conduction band. At room temperature, some of these covalent bonds are broken and the electron can go into a higher energy state in the conduction band, becoming a free particle. It leaves behind a vacancy, which can be filled by one of the neighbouring electrons, shifting the vacancy location. This can be considered to be a positively charged particle called a *hole*. It occupies a valence energy state in the same way a valence electron would do. Both the electron and the hole are free charge carriers and are available for conduction. [28]

Semiconductors are defined to have a *band gap* between the valence and conduction band of $E_g = E_{cond.} - E_{val.} \leq 3.2\,eV$. This energy is chosen since it corresponds approximately to the energy of 400 nm photons, which is 3.11 eV. Therefore, at a temperature of 0 K (no thermal energy of electrons), there are still electrons in the conduction band when illuminated with visible light [29]. In metals the valence and conduction bands overlap, leading to a high conductivity in metals. The band gap of silicon is only $E_g = 1.12\,eV$ [28], but due to energy lost in the lattice structure, the average energy needed to bring an electron into the conduction band, and to thereby generate a hole, is $\langle E_{e,h} \rangle = 3.6\,eV$ [25].
Until now, only pure semiconductors (*intrinsic semiconductors*) have been discussed. Small amounts of impurities (*dopants*) can be added to an intrinsic semiconductor in order to alter the semiconductor's properties, making it an *extrinsic semiconductor*. Some lattice atoms can be replaced by *donor* ions with extra valence electrons or *acceptor* ions with less. This process is called *doping* and generates either *n-type* (adding donors) or *p-type* (adding acceptors) semiconductors. Doping can be modelled as adding localised energy levels in the band gap. If the energy levels from the donors (acceptors) are close to the conduction (valence) band, the states will be almost completely ionised (filled) at 300 K as seen in Figure 2.4. Therefore, many electrons (holes) are in the conduction (valence) band. As there is a higher concentration of free charge carriers compared to the intrinsic semiconductor, the conductivity is increased. Typical dopants for p-type silicon semiconductors are germanium and boron, while phosphorous or arsenic are used for n-type semiconductors.

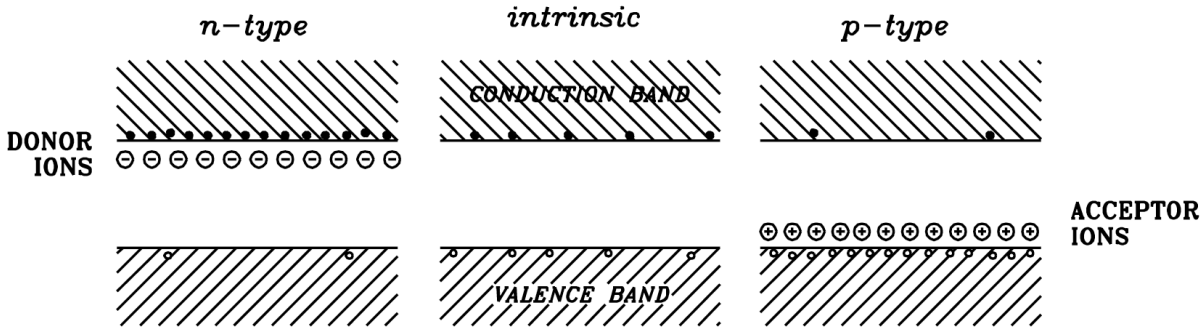

Figure 2.4: Energy band representation of n-type, intrinsic and p-type semiconductors taken from [28]. The energy levels of the donor (acceptor) close to the conduction (valence) band lead to almost completely ionised (filled) states.

A semiconductor can be doped with two different dopants. As one side is p-doped and the other is n-doped, this structure is called a *p-n junction*. Some electrons (holes) from the donors (acceptors) close to the border between the two doping regions diffuse from the n-doped (p-doped) to the p-doped (n-doped) region as seen in Figure 2.5. This leads to an excess of negative charge in the p-type region and of positive charge in the n-type region, producing an electrical potential difference called the *built-in voltage* V_{bi} across the p-n junction. This creates an electric field that counteracts diffusion and also sweeps

away any mobile charge carriers in between the p- and n-type regions [28]. This region void of free charges is called the *depletion region*.
By knowing the acceptor and donor concentrations (N_A and N_D respectively) and V_bi of a p-n junction, one can calculate the depth of the depletion region, the *depletion depth*. Under the assumption of parallel field lines as in [28] the depletion depth is given by:

$$d = \sqrt{\frac{2\epsilon_\mathrm{sc}\epsilon_0(N_\mathrm{A}+N_\mathrm{D})}{eN_\mathrm{A}N_\mathrm{D}}(V_\mathrm{bi}-V_\mathrm{bias})}\,. \tag{2.3}$$

ϵ_0 and ϵ_sc are the vacuum and relative permittivity. V_bias is an additional bias voltage applied over the p-n junction in order to increase the depletion depth. If one of the dopants has a much higher concentration than the other ($N_\mathrm{D} \gg N_\mathrm{A}$ as in the H35 demonstrator chip pixels, see Section 2.5), Equation (2.3) simplifies to

$$d \approx \sqrt{\frac{2\epsilon_\mathrm{sc}\epsilon_0}{eN_\mathrm{A}}(V_\mathrm{bi}-V_\mathrm{bias})} = \sqrt{2\epsilon_\mathrm{sc}\epsilon_0\mu\rho(V_\mathrm{bi}-V_\mathrm{bias})} \tag{2.4}$$

where the bulk resistivity $\rho = 1/(e\mu N_\mathrm{A})$ is introduced with μ the mobility of the charge carriers in the semiconductor. The latter is $1350\,\mathrm{cm}^2\,\mathrm{V\,s}$ for electrons and $450\,\mathrm{cm}^2\,\mathrm{V\,s}$ for holes in silicon [24]. ρ is usually given in units of Ωcm.
A p-n junction behaves as a diode and therefore has an I-V (current-voltage) curve as shown in Figure 2.6. It can be biased either with a *forward* (positive) or *reverse bias* (negative) voltage. Silicon sensors work in reverse bias as the depletion depth can be enhanced by Equation (2.4). Under increasing reverse bias, the leakage current grows only slowly. When the breakdown voltage V_BR is reached, the leakage current increases rapidly.

2.3 Silicon detectors: Principle and features

When a charged particle travels through the depletion region of a semiconductor, it generates electron-hole pairs by ionisation as described by Equation (2.1). By knowing $\langle \mathrm{d}E/\mathrm{d}x\rangle_\mathrm{Ion.}$ from Bethe-Bloch (Equation (2.1)), the depletion depth d and the average energy needed to generate an electron-hole pair $\langle E_\mathrm{e,h}\rangle$, the average number of electron-hole pairs created in the depletion region can be calculated as:

$$\langle N\rangle = \frac{\left\langle \frac{\mathrm{d}E}{\mathrm{d}x}\right\rangle_\mathrm{Ion.} d}{\langle E_\mathrm{e,h}\rangle}\,. \tag{2.5}$$

For a depletion depth of 100 μm, this results in a value of $\langle N\rangle \approx 10800$ assuming a MIP with charge ± 1 crossing a silicon detector orthogonally with $-\frac{\mathrm{d}E}{\rho\mathrm{d}x} = 1.661\,\mathrm{MeV\,cm}^2$ for silicon as calculated with PSTAR [31]. Because the fraction of deposited energy used for the creation of an electron-hole pair fluctuates, $\langle N\rangle$ has a variance of [25]

$$\left\langle \Delta N^2\right\rangle = F\cdot\langle N\rangle\,, \tag{2.6}$$

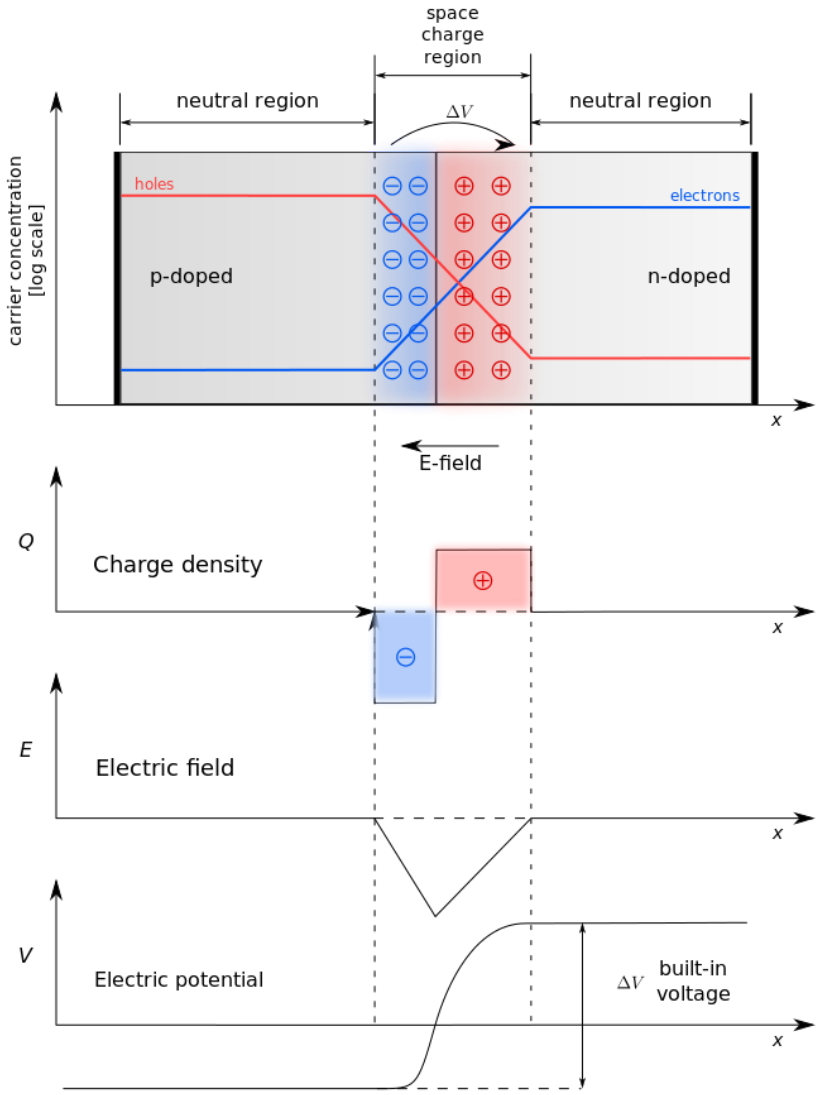

Figure 2.5: A p-n junction in thermal equilibrium with no bias voltage applied taken from [30]. Electron and hole concentrations are depicted with blue and red lines. The grey regions are charge neutral, while the red and blue zones are positively and negatively charged. The excess of negative charge in the p-type region and of positive charge in the n-type region leads to an electrical potential difference called the built-in voltage. It creates an electric field that sweeps away mobile charge carriers in the p-n junction. This is the depletion region.

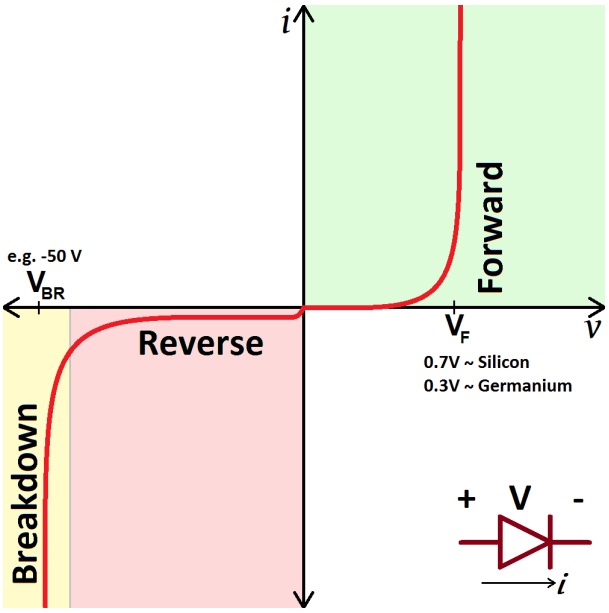

Figure 2.6: I-V curve of a diode taken from [30]. Silicon sensors are operated under reverse bias, for which the leakage current increases only slowly when operated below the breakdown voltage.

where F is the Fano factor [32]. For most semiconductors, it is ~ 0.1. Because of this small Fano factor, semiconductors are capable of measuring the energy loss due to ionisation precisely. In the above example, this leads to a value of $\langle N \rangle \approx 10800 \pm 33$. Furthermore, the dependence of the energy loss on the sensor thickness (as described in Section 2.1) also has to be taken into account.
Because the depletion region is void of free charges, the electrons and holes can drift without recombination towards the electrodes of the semiconductor. Recombination is the process where a free electron fills a hole, thus reducing the number of drifting charge carriers. More details about recombination can be found in [33]. The drift velocity is proportional to the electric field $\vec{E}$ [28]

$$\vec{v}_\mathrm{e} = -\mu_\mathrm{e}(|\vec{E}|) \cdot \vec{E} \quad \text{and} \quad \vec{v}_\mathrm{h} = \mu_\mathrm{h}(|\vec{E}|) \cdot \vec{E}\,. \tag{2.7}$$

The electric fields are of the order of $\sim 100\,\mathrm{V}/100\,\mu\mathrm{m} = 10^6\,\mathrm{V/m}$, which leads to $|\vec{v}_\mathrm{e}|$ of $\sim 135\,\mu\mathrm{m/ns}$.
This movement of charges induces a current, which is measured by the electrodes and amplified. It is proportional to the number of produced electron-hole pairs per unit length and to the depletion depth. This makes the depletion depth a key characteristic of a semiconductor detector.
Semiconductor detectors are used for tracking of charged particles for multiple reasons. Firstly, the low average energy to create an electron-hole pair leads to many charge carriers per unit energy loss of the ionising particle. Because of this, semiconductor detectors have a high signal-to-noise ratio. Furthermore, the high density of the semiconductor

material leads to a large energy loss per traversed length of the ionising particle. Hence, it is possible to build thin detectors which generate large signals. This is important to suppress multiple scattering, which adds a random component to the particle path [20] and therefore contributes to the uncertainty on the track reconstruction. Semiconductor detectors also fulfil the requirement of fast signal generation ($\sim 10\,\text{ns}$) as electrons and holes can move freely in the semiconductor's depletion region. Lastly, they can be produced with a very high granularity, of the order of $100\,\mu\text{m}$. This is important as it allows to distinguish tracks in a high pile-up environment.
The ITk detector uses silicon sensors as they have a small material budget, a high signal-to-noise ratio, are radiation hard and are easily coupled to read-out electronics.

2.4 Radiation damage

Silicon detectors are widely used in high radiation environments such as in space applications, high energy physics and nuclear experiments. Radiation damages the lattice of the semiconductor. This section discusses the processes that damage the bulk lattice of the semiconductor, and how this damage on the lattice affects the properties of the sensor [28].
Hadrons or energetic leptons can displace a *primary knock-on atom* (PKA) in the semiconductor [34]. This leads to them being in-between regular atom sites (*interstitials*) and missing from their original site (*vacancies*). They can migrate through the material and form point defects. If the recoil energy (E_R) of the PKA is high, this can lead to defect clusters, which are dense accumulations of point defects at the end of a recoil track. This is the case for recoil energies of $2\,\text{keV} < E_\text{R} < 12\,\text{keV}$, where one defect cluster and additional point defects are produced. For higher E_R, multiple defect clusters and point defects are created. At low recoil energies of $\lesssim 1\,\text{keV}$ to $2\,\text{keV}$, only isolated point defects are created. Due to this dependence of the type of damage on E_R, the energy of the incident radiation has a significant influence. [28]
Table 2.1 shows some characteristics of the primary interactions of different 1 MeV particles in silicon. The recoil of electrons has a small mean energy (T_av) and needs a lot of energy for the generation of defects (E_min). Therefore, electrons do not produce many defects in silicon. The interactions of hadrons are very different. Their high T_max and low E_min means that recoils can have a lot of energy and not much recoil energy is needed to create defects, thus hadrons generate a lot more defects than electrons. The difference between protons and neutrons is that protons have a much smaller mean recoil energy T_av. This is the case since they also undergo Coulomb scattering, because of which they do not get close to the target nuclei on average. They mostly perform soft collisions with the nuclei. From these observations, it is clear that the primary interaction of radiation is highly dependent on its type and energy. However, this dependency is largely smoothed out by the secondary interaction of a PKA presented in the rightmost column in Table 2.1 [28]. The E_min to create a point defect with a recoil is called the displacement threshold energy E_D, which is approximately 25 eV in silicon [35].
Because of this smoothing out, the primary interaction it not major any more and radi-

Radiation	Electrons	Protons	Neutrons	Si^+
Interaction	Coulomb scattering	Coulomb and nuclear scattering	Elastic nuclear scattering	Coulomb scattering
T_{max} [eV]	155	133700	133900	1000000
T_{av} [eV]	46	210	50000	265
E_{min} [eV]				
point defect	260000	190	190	25
defect cluster	4600000	15000	15000	2000

Table 2.1: Characteristics of primary interaction of radiation and knock-on atoms with silicon taken from [28]. The radiation energy is assumed to be 1 MeV. T_{max} is the maximum kinematically possible recoil energy, T_{av} the mean recoil energy and E_{min} the minimum radiation energy needed for the creation of a point defect and for a defect cluster.

ation damage can be scaled from one type and energy of radiation to another, assuming that the displacement damage induced change in the material is proportional to the energy imparted in displacing collisions, which is the *non-ionising energy loss* (NIEL). It is expressed by the displacement damage cross-section $D(E)$ [34]. This assumed proportionality between the NIEL and the resulting damage effect is called the *NIEL-scaling hypothesis* [36].
$D(E)$ is usually normalised to 1 MeV neutrons as they only cause non-ionising damage. The scaling factor between different types and energies of radiation is the hardness parameter $\kappa(E)$, shown in Figure 2.7 for particles of different energies. For 1 MeV neutrons $\kappa = 1$. Protons have a strongly growing κ for $E < 10$ MeV. This is due to the Coulomb interaction of the protons [34]. For high energies, the contribution from Coulomb scattering decreases, and neutrons and protons behave very similarly.
The interstitials and vacancies produced by radiation are mobile at room temperature and an interstitial fills the place of a vacancy or the defects diffuse out of the surface. This is known as *annealing*. The defects are not present anymore and the semiconductor can recover from the radiation damage.
Not all defects are vanishing in this way. Some interact with other defects, dopants or oxygen remaining from the crystal-growing process and become defect complexes that are immobile at room temperature. They act as recombination-generation centres, leading to an increase of the reverse-bias current in the depletion region. The defect complexes can also act as trapping centres in which free charge carriers get captured and re-emitted, adding a time delay. If this happens in the depletion region and the delay is too long, the signal can be reduced as less charges are drifting in the detection period. Lastly, defect complexes can modify the effective concentration of donors and acceptors thus changing the depletion depth according to Equation (2.4). For example, some original boron dopants can be captured into defect complexes. As they lose their original function as acceptor, this is an effective removal of acceptors. Such a change in the dopant concentrations can also be beneficial, since $d \propto \sqrt{1/N_A}$ (for $N_D \gg N_A$) [34, 37].
As defect complexes cannot be perfectly modelled, parametrisations are used in order

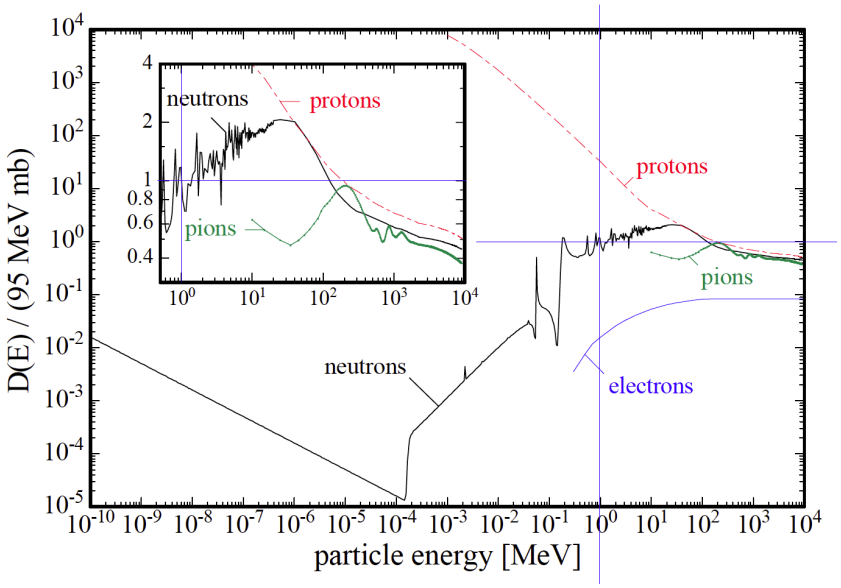

Figure 2.7: Damage function $D(E)$ normalised to 1 MeV neutrons for protons, neutrons, pions and electrons in silicon taken from [36]. The damage function describes the damage effect due to displacements of lattice atoms. When normalised to 1 MeV neutrons, it is equivalent to the hardness parameter κ, as indicated by the blue lines.

to describe the changes of the semiconductor's macroscopic properties as a function of NIEL. The effective doping concentration can be parametrised as:

$$N_{\text{eff}}(\Phi) = N_{\text{D},0}e^{c_{\text{D}}\Phi} - N_{\text{A},0}e^{c_{\text{A}}\Phi} + b_{\text{D}}\Phi - b_{\text{A}}\Phi\,. \tag{2.8}$$

$N_{\text{D},0}$ and $N_{\text{A},0}$ are the donor and acceptor concentrations before irradiation and c_{D}, c_{A}, b_{D} and b_{A} are experimentally determined constants.

2.5 Monolithic sensors and the H35 demonstrator chip

The standard operation of silicon sensors in particle physics experiments is using a *hybrid* chip design. In such designs the sensing semiconductor is either bump bonded or glued, and wire-bonded to a front-end chip. This technique is used in most silicon detectors as for example in the current ATLAS Inner Detector [38] and its Insertable B-Layer [11]. In contrast to this, the in-pixel analog and digital electronics are included in the sensor itself in monolithic sensors.
High voltage CMOS (HV-CMOS) is a reliable technology frequently used in the industry, but still relatively new to the field of particle physics and offers the opportunity to produce monolithic sensors. This is possible by putting the pixel electronics into deep n-wells, shielding them from the high voltage [39]. The possible omission of bump-bondings and the use of commercial technologies in monolithic sensors make HV-CMOS sensors an economical alternative to standard hybrid detectors. Furthermore, it simplifies the

production, reduces the amount of material in the detector and the sources of malfunction. HV-CMOS allows for the application of reverse bias voltages of the order of −100 V. This leads to a large depleted volume and fast charge collection since the main contribution to the charge carrier movement comes from drift and not from diffusion [15].
Monolithic HV-CMOS sensors are considered for the outer pixel layers of ATLAS ITk, where the requirements for radiation hardness and hit rate are not as stringent as in the innermost layers [13]. In this study, the H35 demonstrator chip prototype [40] is being characterised. Chips of the four substrate resistivities 20, 80, 200 and 1000 Ω cm were produced by the ams AG foundry in the 350 nm HV-CMOS process [41]. Three deep n-wells are implanted in a p-substrate (*n in p* design, $N_D \gg N_A$), forming p-n junctions as shown in Figure 2.8. The nMOS and pMOS transistors are embedded in the central deep n-well and act as collecting electrodes.

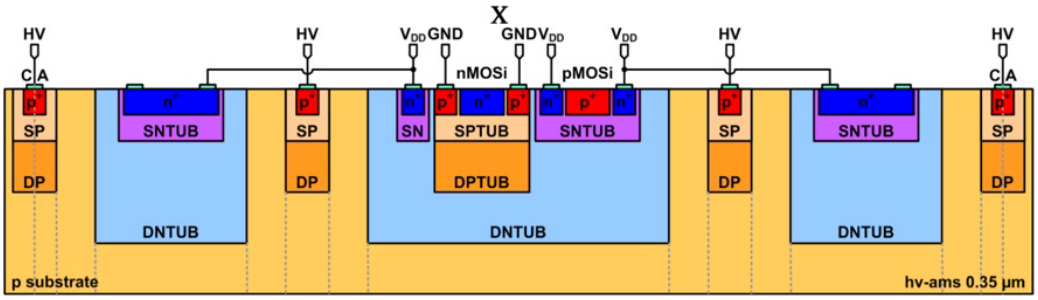

Figure 2.8: Cross section of a pixel produced in the 350 nm HV-CMOS process taken from [42]. The layers p^+ and n^- are diffusion implants, while SNTUB and DNTUB mark the shallow and deep n-wells. In the same manner, SPTUB and DPTUB are the shallow and deep p-wells. The deep n-wells embedded in the p-substrate form p-n junctions, therefore acting as electrodes. Since the pixel electronics are embedded in the central deep n-well, they are shielded from the high voltage [39].

On the H35 demonstrator chip there are two analog and two digital pixel matrices as seen in Figure 2.9. On the bottom of the chip, there is a test matrix dedicated for Transient Current Technique (TCT) studies. It consists of nine pixels with dimensions of $250 \times 50\,\mu m^2$ each. The eight outer pixels are shorted together. For the following studies, only the inner pixel is considered.
In the next chapter, the TCT used for the characterisation of the H35 demonstrator chip is discussed.

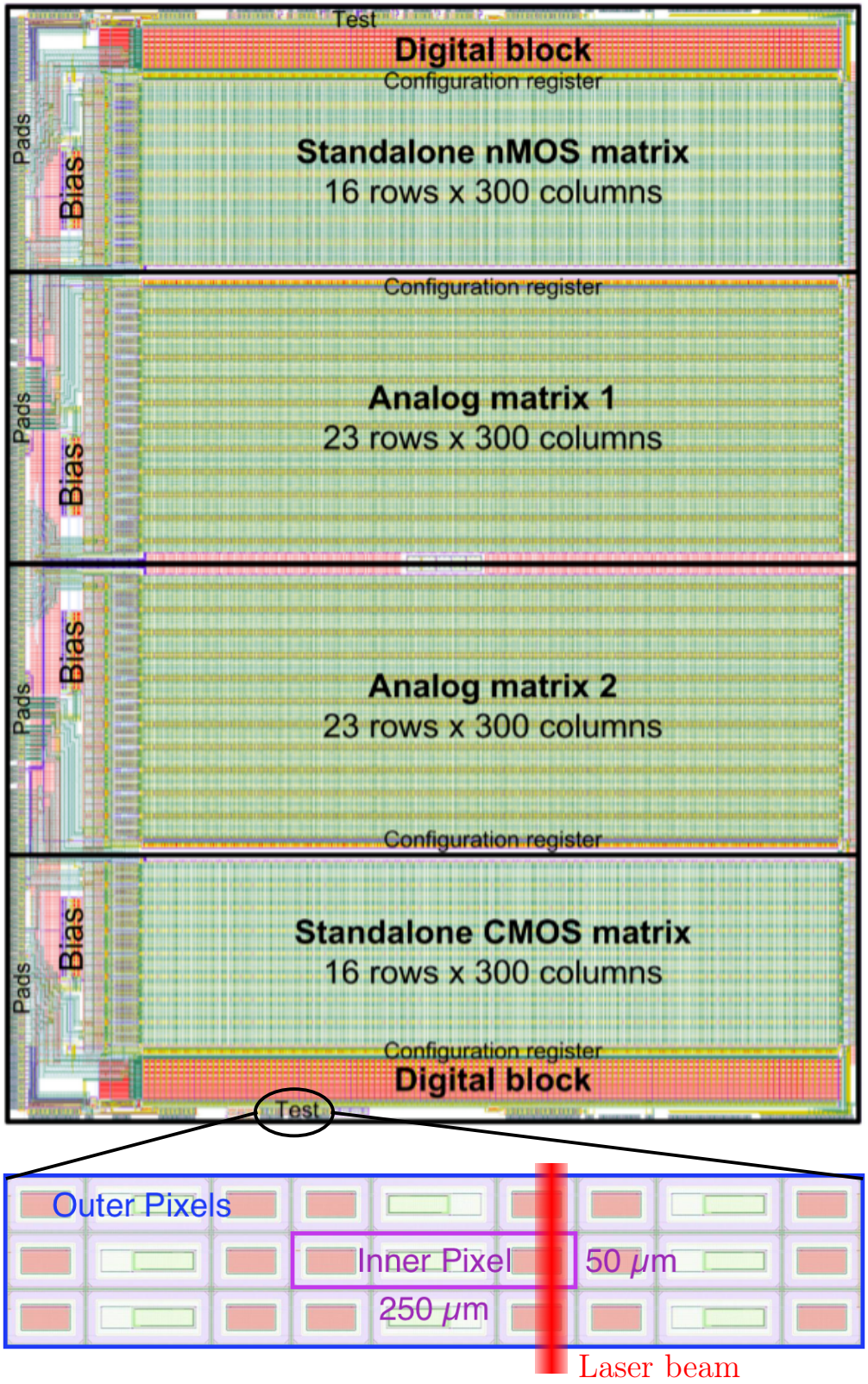

Figure 2.9: Top view of the H35 demonstrator chip (top) taken from [40] and close-up of its test matrix dedicated for TCT studies (bottom). The laser beam (red, not to scale) comes from the bottom and penetrates the test matrix pixels along their width of 50 µm (referred to as the edge-TCT configuration, see Section 3.1).

Chapter 3

Transient Current Technique measurements

The Transient Current Technique (TCT) is used to characterise the bulk properties of solid state detectors. In this study, edge-TCT [43] is utilised to measure the depletion depth in the H35 demonstrator chip. This chapter explains the principle of TCT and presents the experimental setup. Subsequently, details about the device under test are presented. Lastly, the calculation of the depletion depth and results of non-irradiated H35 demonstrator chips are described.

3.1 Principle of Transient Current Technique

In a semiconductor detector, signals are induced in the electrodes by the motion of free carriers in the bulk. A discussion about particle interaction with silicon can be found in Section 2.1.
The principle of TCT is illustrated in Figure 3.1. It consists of inducing a signal in a known position of the device in order to reconstruct the depletion region of the sensor. In the case of this thesis, the device under test (DUT) is illuminated with focused light pulses from a laser. If the photons have an energy higher than the band gap of the semiconductor, free carriers are generated in its bulk. The laser is injected at different sample coordinates with micrometric precision, while the DUT is reverse biased to different voltages. In the depleted region of the DUT, the injected free charge carriers drift under the electric field of the semiconductor and induce a current in the electrodes of the DUT. This signal is amplified by a charge-sensitive amplifier, giving a voltage pulse. In this way, the TCT maps the sensitive area (depletion region) of the DUT.
In order to measure the depletion depth, the sensor is illuminated by the laser from its edge referred to as *edge-TCT*. This gives information about the structure of the depletion region in the sensor's depth. The depletion depth then is defined as the full width half maximum (FWHM) of the signal profile in depth.
To resolve the structure of the depletion region, the laser beam spot size must be smaller than the features to be probed. A narrow beam spot is accomplished by using a single

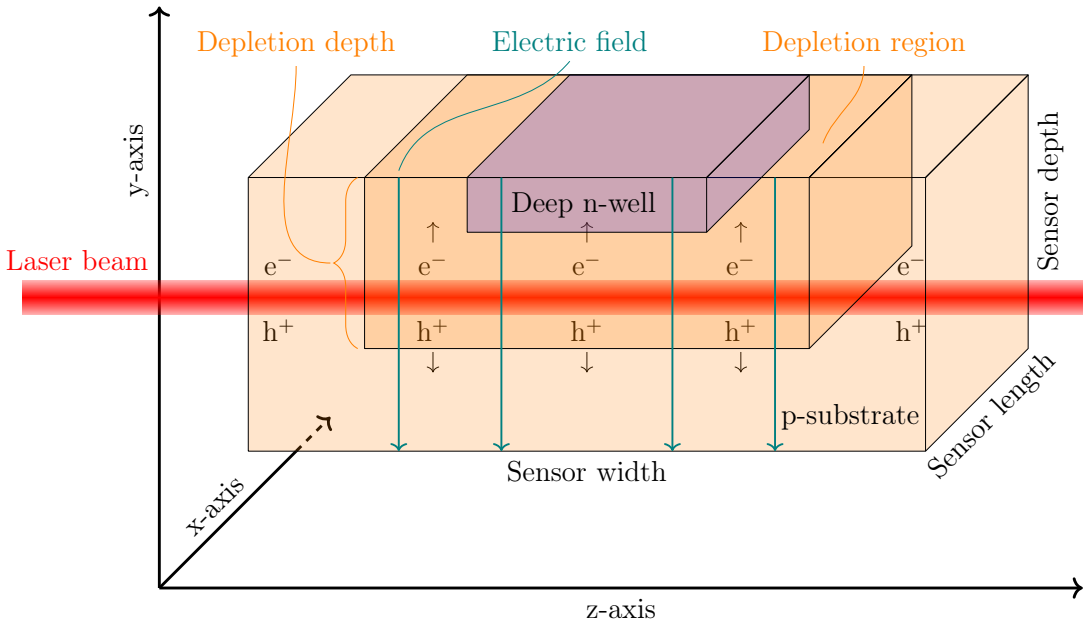

Figure 3.1: Working principle of edge-TCT in a back-biased n in p semiconductor. In between the p-substrate and the deep n-well, there is the depletion region. The laser is pointed onto the edge of the sensor and creates electron-hole pairs along the ray. In the depletion region, the electron and hole are free charge carriers and drift towards the electrodes due to the electric field. This induces a current signal in the electrodes. The sensor is mounted on a stage and is scanned in x (length) and y (depth).

mode optical fibre coupled to an optical system. For a more detailed description of TCT, please refer to [44].

3.2 Transient Current Technique setup

The TCT setup used for this study is a Scanning-TCT from Particulars [45] and is shown in Figure 3.2.
It hosts a LA-01 IR FC model [46] pulsed laser with a wavelength of 1060 nm. The photons therefore have an energy of $E = hc/\lambda = 1.17\,\text{eV}$ which is sufficient to overcome the band gap of $E_\text{g} = 1.12\,\text{eV}$ in silicon and promote an electron to the conduction band, also generating an hole.
The laser system is controlled remotely via a computer and generates also a trigger signal on the pulse production. By having a very short pulse width of 440 ps, the laser generates a similar signal as a MIP passing through the detector. The pulse frequency is 10 kHz and allows the averaging of a big number of signals to be taken for a single DUT coordinate. The laser is coupled to a single mode optical fibre which directs the light to a beam expander which focuses the beam onto the DUT. Both the optical system and the DUT are mounted on stages with 1 µm step size, forming a full 3D translation system. It is

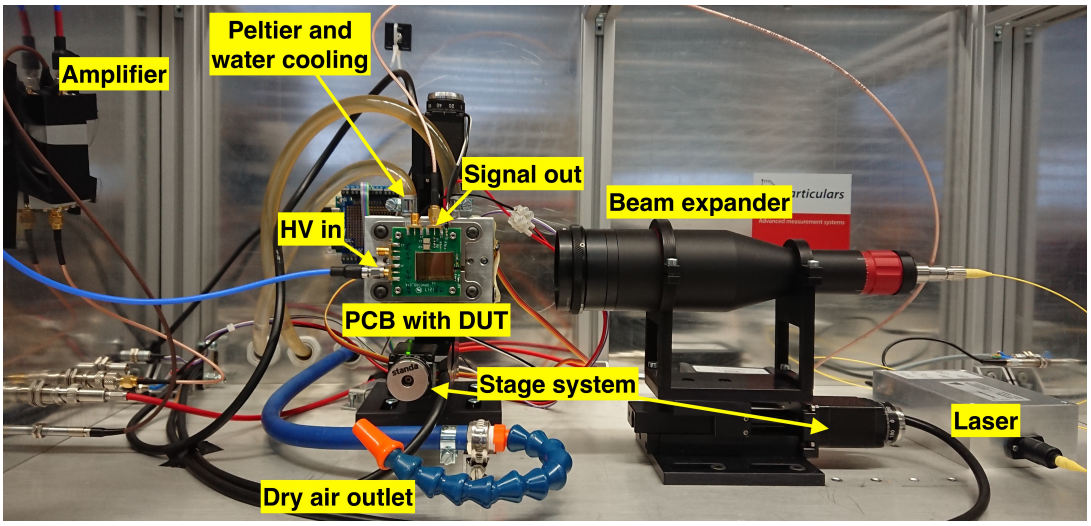

Figure 3.2: Setup of the TCT in edge configuration. The laser light is connected to the beam expander by an optical fibre and is focused on the DUT. They both are mounted on stages, forming a 3D translation system that allows to perform scans with micrometric precision. The DUT is biased by a high voltage power supply (not in this picture). Its signal passes through an amplifier before digitisation. The DUT is cooled by a Peltier cell. The hot side of the latter is connected to a water cooling cycle. During operation, the box is closed and flushed with dry air in order to keep the humidity low.

therefore possible to perform scans with $\sim 1\,\mu m$ resolution and to focus accurately.
The DUT is attached on an aluminium adapter plate which is cooled to reduce the thermal noise. The cooling system consists of a 50 W Peltier cell and a water cooling cycle carrying away the heat from the hot side of the cell. This cooling system allows for temperatures of $\sim -20\,°C$ on the DUT. In order to keep humidity low in the TCT box, it is constantly flushed with dry air.
The DUT is biased by a Keithley 2410 high voltage source [47]. The signal passes to a AM-02 charge-sensitive amplifier from Particulars [48]. This is a wide band width amplifier (0.01–3000 MHz) with an amplification of 53 dB. Downstream of the amplifier, the signal is analysed by a DRS4 Evaluation Board from PSI [49]. It digitises the signal, triggering on the laser trigger signal. The board features a sampling rate of up to $f = 5 \times 10^9\,Hz$ with a time resolution of 0.2 ns. 1024 measurements form a graph that shows the change in the recorded signal. This *waveform* has a length of $\sim 200\,ns$. One hundred of these are averaged to reduce the noise of the voltage signal. The DUT is scanned along y (depth of sensor) and x (length of sensor) and is biased with different voltages. The setup saves a waveform for every scan position and voltage.
By using a different adapter plate, the setup can also perform top-TCT scans where the DUT is illuminated by the laser from the top. In that configuration, the area of the depletion region can be estimated and compared to the total area of the DUT.

3.3 Validation of the setup

Edge-TCT scans can take up to 24 hrs and consist of $\sim$ 100000 single measurements. The laser must be stable over this time scale as the measured signal is proportional to the laser intensity. Furthermore, the beam spot size has to be known as it is the limiting factor for the resolution of structures.
The intensity stability of the laser was monitored downstream of the beam expander with a OP-2 VIS laser power sensor from Coherent [50]. An example measurement is seen in Figure 3.3. The laser intensity was found to vary less than 2%. Hence, no time dependent correction is applied to the scans.

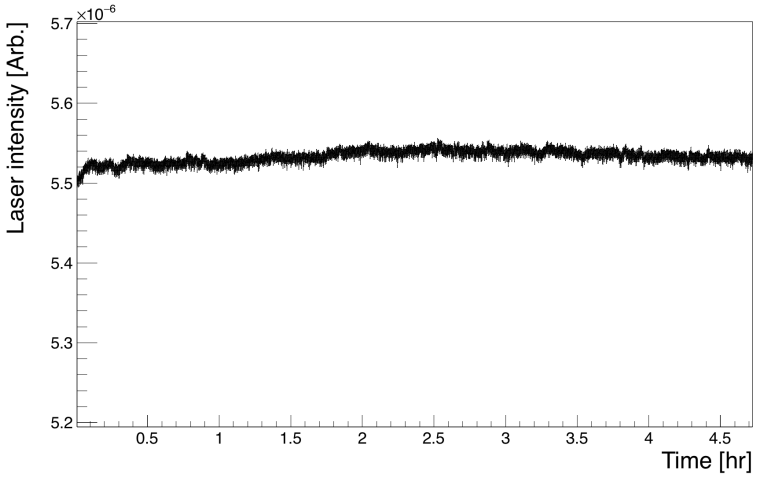

Figure 3.3: Stability of the infrared laser. The intensity of the laser was measured downstream of the beam expander with a OP-2 VIS laser power sensor from Coherent [50]. Variations have been found to be $\leq 2\%$.

The beam spot size of the infrared laser was measured by utilising a strip diode. It has a silicon pad that is covered with metallised lines, which block the laser light. Signals were recorded by scanning over the sharp edge of one metallised line for different positions of the laser on the focal axis. The steepness of this transition depends on the beam spot size. The larger it is, the more the transition gets smoothed out. This transition is fitted with an error function $\mathrm{erf}\,(z) = \frac{2}{\sqrt{\pi}} \int_0^z e^{-t^2} \mathrm{d}t$ as given in [51]. Assuming a Gaussian intensity distribution of the laser, the FWHM of the beam spot can be obtained from the parameters of the fit. Figure 3.4 shows the FWHM of the beam in dependence of the laser position on the focal axis. The minimal FWHM of the beam spot was measured to be $15 \pm 2\,\mu\mathrm{m}$.

3.4 Samples tested

Samples of the resistivities 20, 80, 200 and 1000 $\Omega\,$cm of the H35 demonstrator chip are glued and wire bonded on a dedicated PCB, which matches the input impedance of the

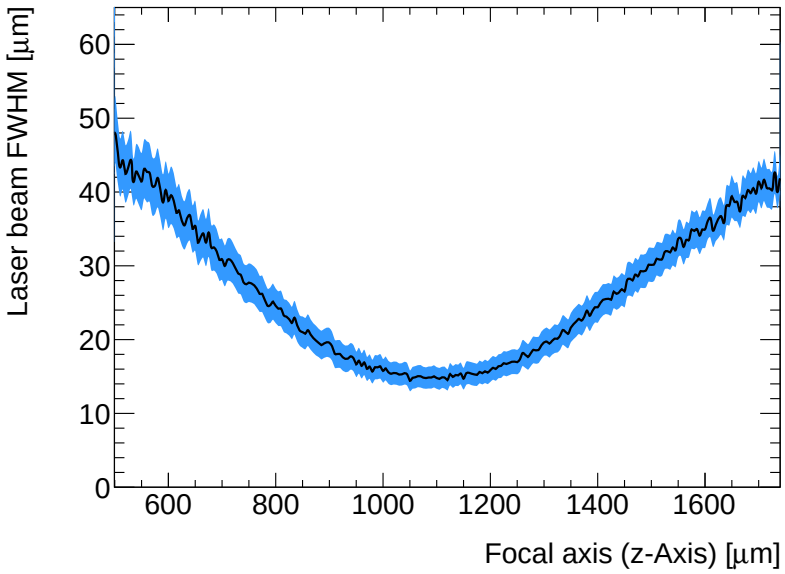

Figure 3.4: FWHM of the laser received from an error function fit on the collected charge over a sharp edge for different z. The minimal FWHM is $15 \pm 2\,\mu\text{m}$, which is a limiting factor to resolve structures.

amplifier and cables with the output impedance of the sensor. The PCB allows for the read out either the central pixel or the eight outer pixels of the test matrix. The pixels are reverse-biased with a high voltage (up to $-100\,\text{V}$). Higher voltages are not considered. The irradiation study was completed with one sample per resistivity, simulating the continuous radiation in the sensor's lifetime in HL-LHC.
Using an infrared laser allows for a nearly constant electron-hole production along several hundred micrometer of silicon, because the attenuation length of 1060 nm light in silicon is $\sim 1\,\text{mm}$ as seen in Figure 3.5. This is needed since the central test matrix pixel of the H35 demonstrator chip is behind an outer pixel as shown in Figure 2.9.

3.5 Depletion depth calculation

This section describes how the depletion depth is calculated from the scan files saved by the TCT. The data analysis was written in C++ using packages from the ROOT framework [52] and the TCTAnalyse library from Particulars [53].
The TCT saves one averaged waveform for each scanned position. An example is depicted in Figure 3.6. The baseline (offset of the signal from zero) of the waveform is corrected and the voltage signal is integrated over 8 ns to get the induced charge.
Iterating over the length and depth of the sensor gives a two-dimensional image of the depletion region as shown in Figure 3.7, where the bin contents are the induced charge at the corresponding positions.
The depletion depth is defined as the FWHM of the depth profile (columns in Figure 3.7).

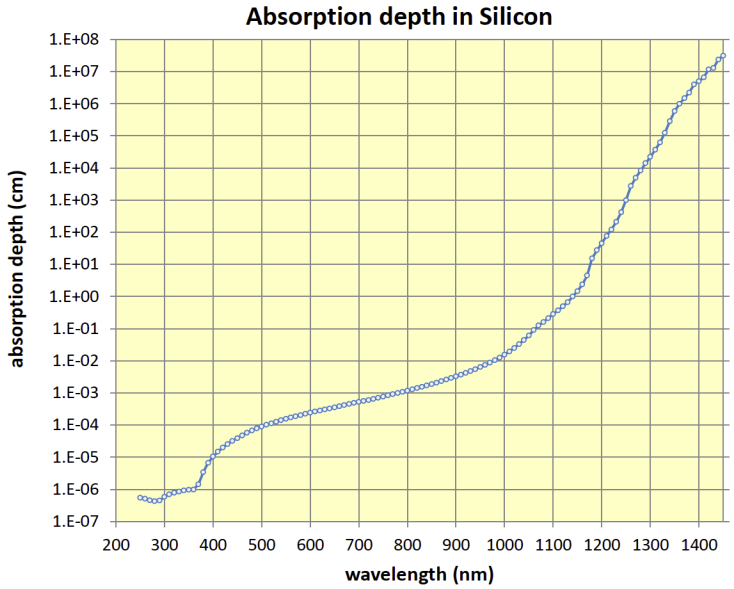

Figure 3.5: Optical absorption of silicon at 300 K taken from [44]. The absorption depth is equivalent to the attenuation length and is ~ 1 mm for 1060 nm photons. Due to this high attenuation length, the generation of electron-hole pairs is nearly constant along a few hundred micrometers of silicon.

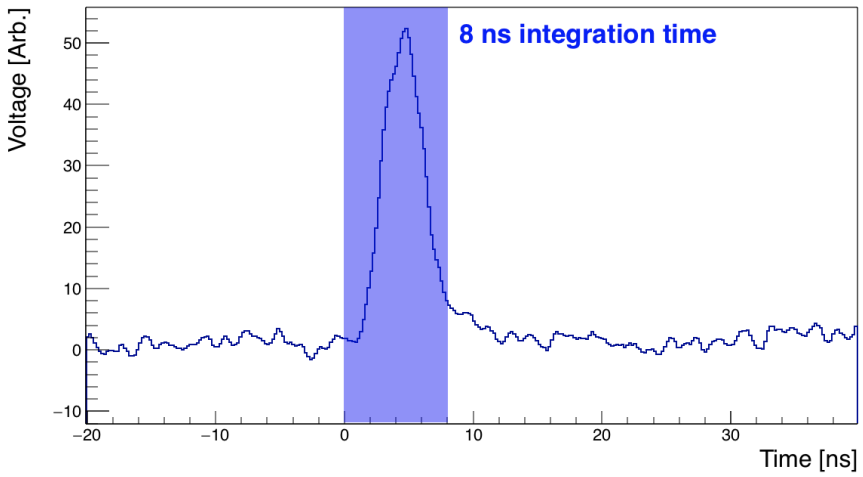

Figure 3.6: Example waveform produced by the setup. The waveform is an average of 100 independent measurements in order to reduce noise. The blue area marks the integration window of 8 ns used in the analysis. The total waveform consists of 1024 points over ~ 200 ns.

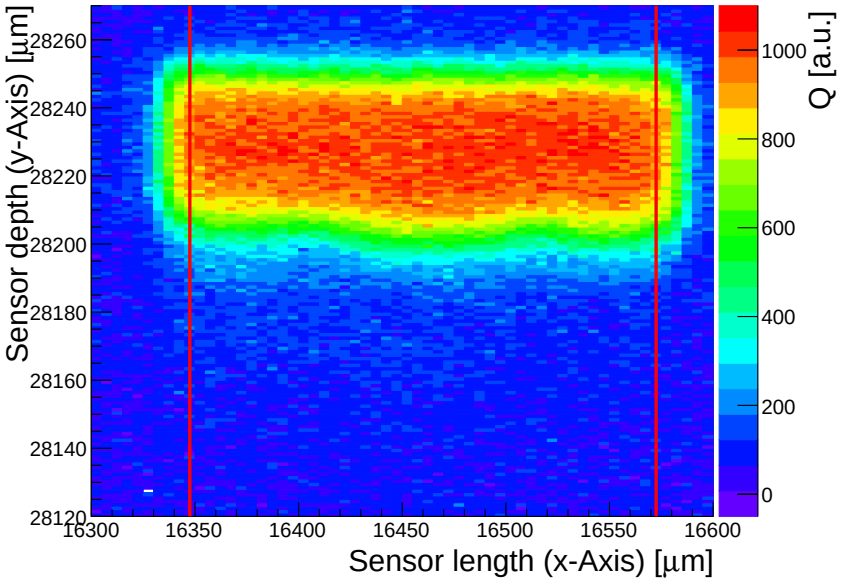

Figure 3.7: Two-dimensional scan of the depletion region of a non-irradiated 200 Ωcm H35 demonstrator chip at $V_{\text{bias}} = -80\,\text{V}$ recorded with edge-TCT. Each column represents one depth profile of the depletion region. The red lines mark the first and last depth profiles selected for the depletion depth calculation.

As the scans also cover some non-depleted area around the depletion region, a selection on the profiles is applied. Depth profiles with an average induced charge below a threshold are rejected. The threshold is set to 0.85 times the maximal average induced charge of all the depth profiles. The first and last selected depth profiles are marked by the red vertical line in Figure 3.7.
Figure 3.8 shows example depth profiles for the 200 and 1000 Ω cm resistivity samples at −80 V bias voltage. The depth profiles feature a plateau at small depths. In the profile of the 1000 Ω cm sample, there is a secondary peak at large sensor depths (charge sharing peak), which was previously also observed by [15]. By looking at the depth profile of the outer test matrix pixels, it was concluded that this feature arises from charge sharing. As the laser hits the H35 demonstrator chip from its edge, electron-hole pairs are produced not only in the central pixel, but also in the pixels in the front and back (see Figure 2.9). The electric field lines of these pixels can end on the electrodes of the central pixel for large depths. Free carriers generated deep in the outer pixels of the test matrix can therefore drift towards the electrodes of the central pixel, which induces a current in the electrodes of the central pixel. The contribution of charge sharing increases the charge seen deep in the central pixel and exceeds the drift plateau seen in the 200 Ω cm sample. To calculate the correct FWHM of the depletion region, the maximum from drift of charge carriers generated only in the central pixel has to be considered. In this way the depletion depth results are also comparable with results on neutron irradiated H35 demonstrator chips in reference [15], that observed the same charge sharing phenomenon.

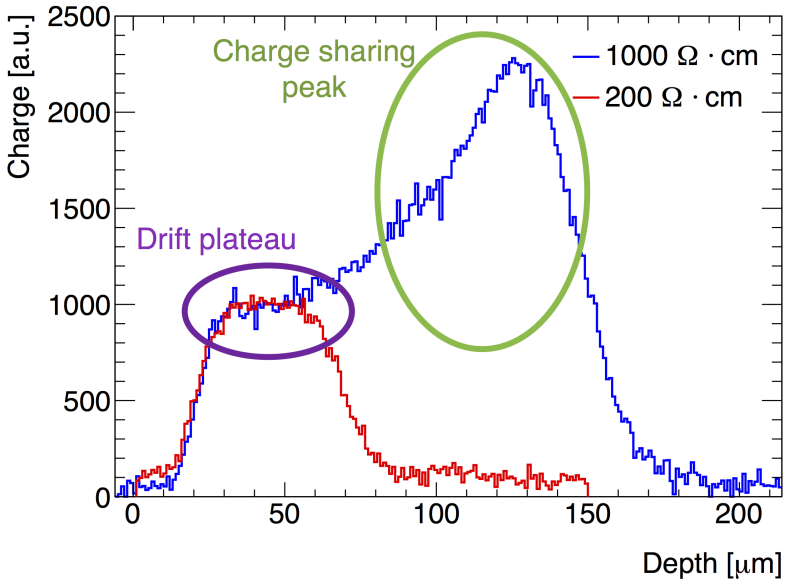

Figure 3.8: Example depth profiles at −80 V bias voltage for the 200 and 1000 Ω cm samples of the H35 demonstrator chip. The depletion depth analysis has to ignore the global maximum (charge sharing peak in green) in the 1000 Ω cm sample and instead find the charge of the drift plateau (marked in violet), which is then used as the maximum for the FWHM calculation.

I solved this issue by fitting the depth profiles with a function that contains one term approximating the expected signal without charge sharing and another term simulating the charge sharing contribution. The product of an error and a conjugate error function ($\mathrm{erfc}(y) = 1 - \mathrm{erf}(y)$ as given in [51]) is chosen to replicate the expected profile in depth y without charge sharing, while the effect of charge sharing is approximated with a Gaussian:

$$f_{\mathrm{fit}}(y) = \underbrace{\frac{A}{4} \cdot \left\{ \mathrm{erf}\left(\frac{y - y_1}{\sigma_1}\right) + 1 \right\} \cdot \mathrm{erfc}\left(\frac{y - y_2}{\sigma_2}\right)}_{\text{Expected depth profile}} + \underbrace{B \cdot \mathrm{Gaussian}\,(y, \sigma, \mu)}_{\text{Charge sharing contribution}} + C \tag{3.1}$$

The product of the error functions simulates a Gaussian smeared rectangular function with y_1 and y_2 being the beginning and end of the pulse. σ_1 and σ_2 define how much the pulse is smeared by the laser's beam spot, while A is the height of the rectangular pulse. B is the height of the charge sharing contribution and σ and μ define its width and position. Lastly, the constant C is added to compensate a possible baseline.
All depth profiles are fitted with f_{fit}. As seen in Figure 3.9, this fit describes both the depth profiles with and without the charge sharing peak well. The amplitude of the depth profile A is taken as the maximum for the FWHM calculation, instead of the global maximum of the depth profile. If $|\mu - y_1| < 1.5 \cdot \sigma$, the depth profile is altogether

Gaussian like and no second Gaussian from charge sharing can be identified. Therefore, the global maximum is taken for the FWHM calculation.

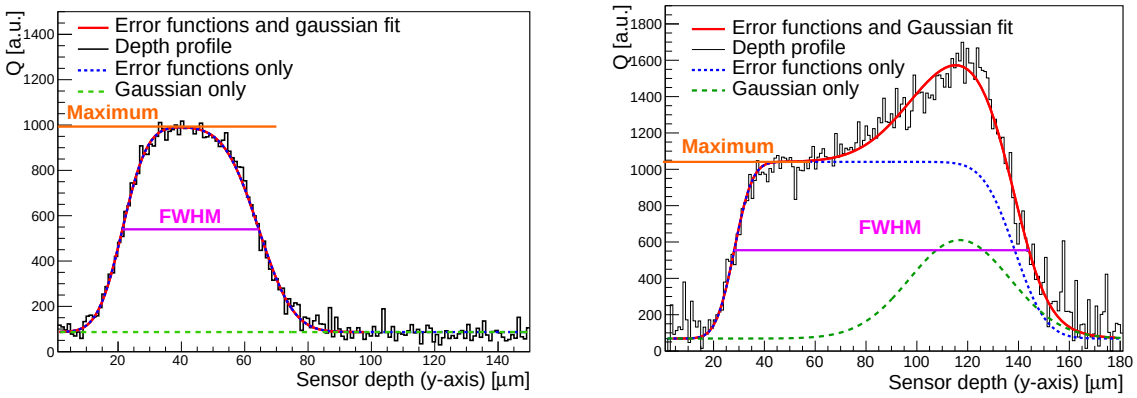

(a) 200 Ω cm sample

(b) 1000 Ω cm sample

Figure 3.9: Example depth profiles from the H35 demonstrator chip at −60 V fitted with Equation (3.1) in red in order to find the correct maximum for the FWHM calculation. The fit function consists of one term for the expected depth profile and one term for the charge sharing contribution, which are shown in blue and green respectively. The charge sharing contribution is zero in the 200 Ω cm sample (a), while it plays a major role in the 1000 Ω cm resistivity case (b). The orange line marks the maximum of the error functions (expected depth profile), which is used for the FWHM calculation. The latter is indicated by the pink line.

Depth profiles with a bad fit are discarded by applying a χ^2 per degree of freedom cut at 20 (30 for 1000 Ω cm samples). Applying above calculation to each depth profile, a distribution of depletion depths for each bias voltage is received. The depletion depth at a certain voltage is then the mean of this distribution and the error is its standard error. The dependence of the depletion depth on the bias voltage for the four resistivities considered is discussed in the following section.

3.6 Characterisation of non-irradiated samples

For each DUT, a focus scan has been performed to ensure that the laser is focused on the central test matrix pixel. As shown in Section 3.3, the FWHM of the laser beam spot is 15 ± 2 µm. The depletion region of the central pixel is scanned with 1 µm step size in depth and 5 µm step size in length for bias voltages from 0 to −100 V. Figure 3.10 shows the 2D plots of the four resistivity samples at −80 V. It can already be seen here that the depletion depth is higher for the high resistivity samples as expected by $d \propto \sqrt{\rho V}$ (see Equation (2.4)) under the assumption of parallel field lines. Furthermore, a length dependence of the depletion depth can be noticed in the 20 and 80 Ω cm samples. More free charge carriers are drifting close to the n-wells.

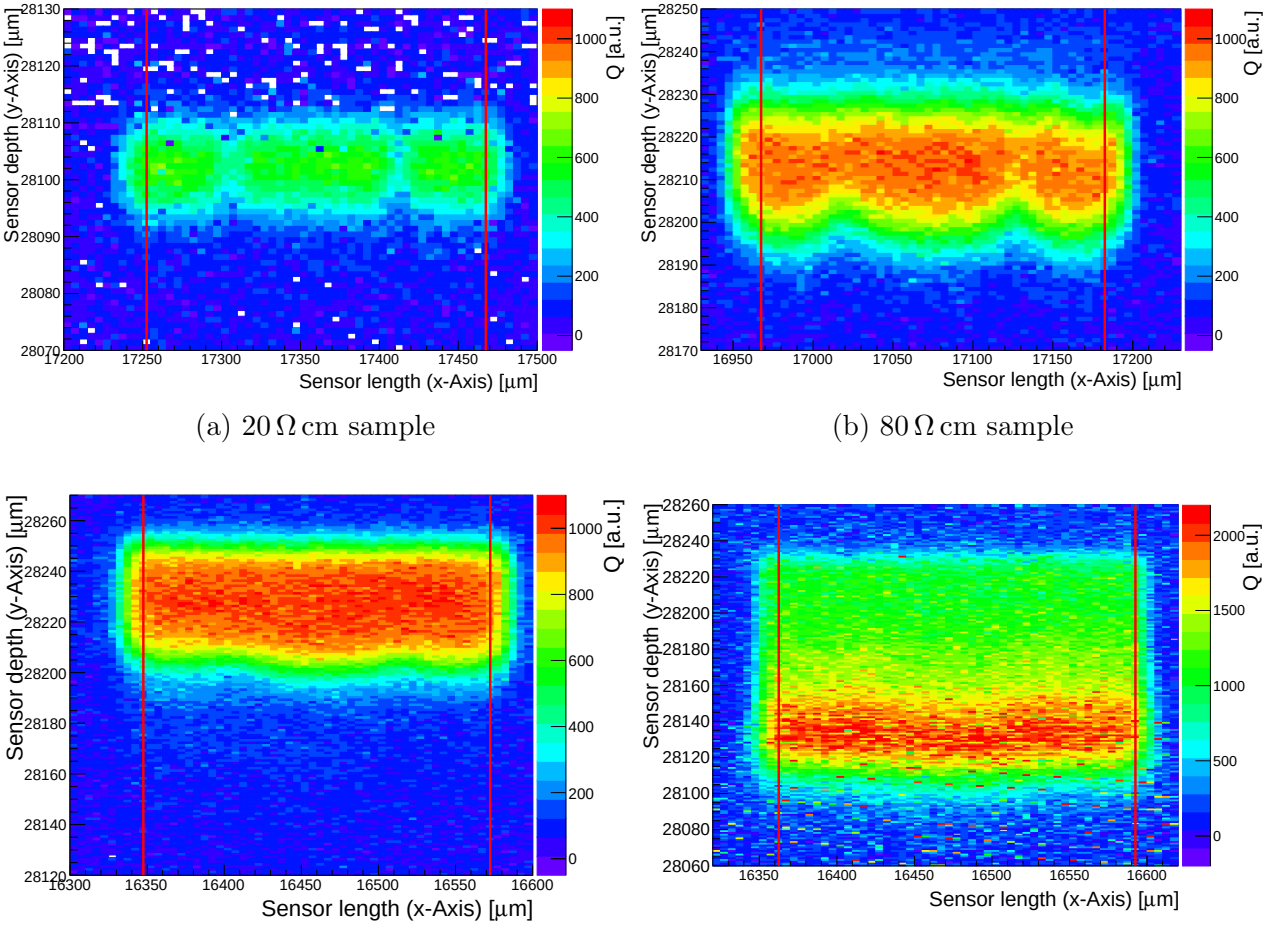

(a) 20 Ω cm sample

(b) 80 Ω cm sample

(c) 200 Ω cm sample

(d) 1000 Ω cm sample

Figure 3.10: Two-dimensional scan of the depletion region for different resistivities before irradiation at −80 V bias voltage. The charge sharing effect is seen by the higher charge deeper in the sensor in (d). The depletion region is deeper in high resistivity samples.

As described in Section 3.5, the depletion depth is the FWHM of the depth profile. Figure 3.11 shows the evolution of the depth profile with bias voltage for resistivities of 200 and 1000 Ω cm at a fixed sensor length. It is seen that the peak coming from charge sharing in the 1000 Ω cm sample starts appearing from −20 V on at high depths. It is furthermore noted that the collected charge of the drift maximum increases with bias voltage up to ∼ −40 V. This is the case since at lower bias voltages the depletion depth is smaller than the laser beam spot size, so that the laser is not fully contained in the depletion region. This decreases the collected charge and limits the spatial resolution of the scans. The lower bound for the minimum FWHM has been found to be limited to 15 µm, which is the beam spot size of the laser.
This resolution limitation can be overcome by using the evolution of the collected charge with bias voltage. The charge grows linearly with the true depletion depth until it reaches a maximum ($Q_{\max}$), since the depletion region is deep enough to contain the whole laser beam spot. Since the true depletion depth d_{true} is proportional to $\sqrt{V_{\text{bias}}}$, the voltage evolution of the collected charge $Q(V)$ can be used to correct the measured depletion depth d by

$$d_{\text{true}}(V) = d(V) \cdot \frac{Q(V)}{Q_{\max}}. \tag{3.2}$$

This method was applied to the depletion depth evolution of the 80 and 200 Ω cm samples, recovering resolution capabilities below 15 µm. The 20 Ω cm sample however can not be corrected in this way as the collected charge never reaches a maximum. This is the case because the depletion depth at the maximal bias voltage still is below 20 µm. Instead, it was corrected by taking the maximal collected charge from the 80 and 200 Ω cm samples. The resulting evolution of the depletion depth with bias voltage is shown in Figure 3.12 for the four different resistivities. The curves are fitted with $d \propto \sqrt{\rho\,(V_{\text{bi}} - V_{\text{bias}})}$ (see Equation (2.4)) under the assumption of parallel field lines. The built-in voltage is limited to $0.2\,\text{V} < V_{\text{bi}} < 0.6\,\text{V}$ to comply with measurements on the samples.
In addition to the study of the depletion depth, also top-TCT scans have been performed. Figure 3.13 shows the induced charge in the 200 Ω cm sample, revealing the structure of the sensor and its active area as seen from above. When compared with the H35 pixel layout in Figure 2.8, the three deep n-wells are recognisable.
The next chapter presents the irradiation campaign with protons at the Bern Cyclotron and the evolution of depletion depth with fluence. These results are then compared with other irradiation campaigns.

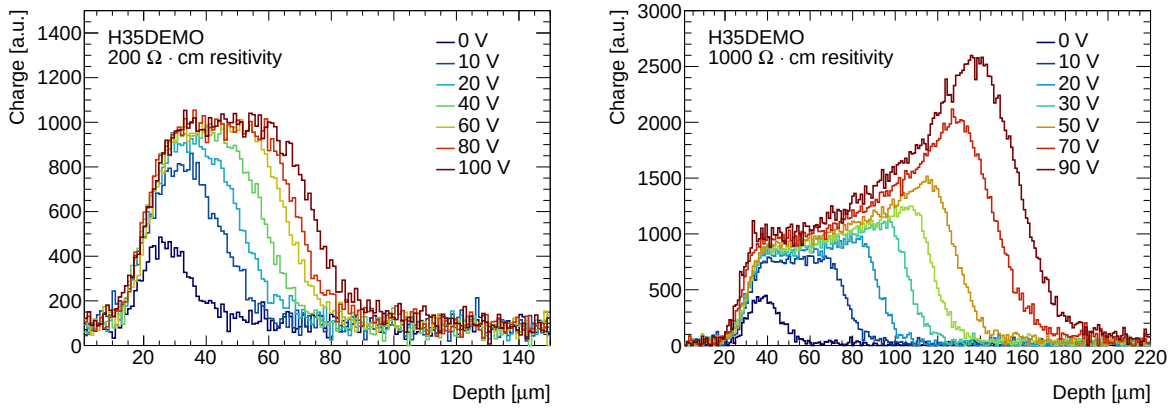

(a) 200 Ω cm sample (b) 1000 Ω cm sample

Figure 3.11: Evolution of the depth profiles with bias voltage at a fixed sensor length. The induced charge is smaller at low bias voltages. The charge sharing effect is seen in the 1000 Ω cm sample seen in (b).

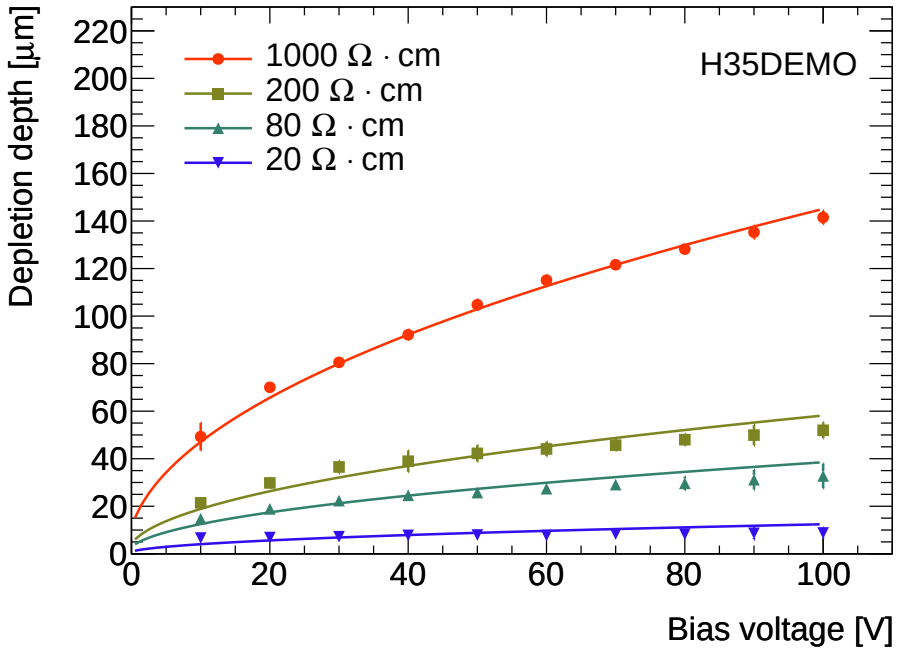

Figure 3.12: Voltage dependence of the depletion depth for different resistivities of the H35 demonstrator chip. The depletion depths are fitted with Equation (2.4) under the assumption of parallel field lines.

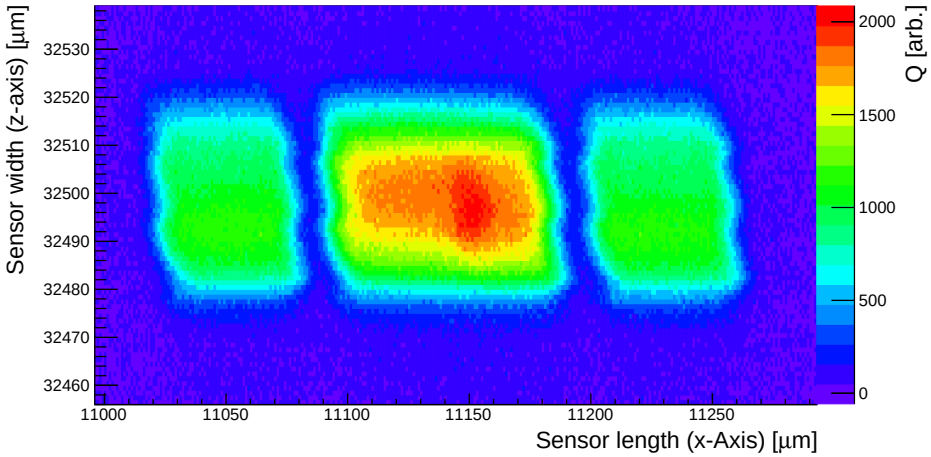

Figure 3.13: Top-TCT scan of the 200 Ω cm sample. The three deep n-wells of the H35 demonstrator chip are recognisable.

Chapter 4

Irradiation campaign at the Bern Cyclotron

For the irradiation of the H35 demonstrator chip with protons, the Bern medical cyclotron [54] was used. Multiple irradiations steps have been performed to a cumulated fluence of $\sim 1.5 \cdot 10^{15}$ 1 MeV n_{eq}/cm^2. In between the irradiations, the depletion depth of the samples has been measured with the TCT. The samples were stored at room temperature. This chapter first describes the Bern Cyclotron facility and the method used to measure the delivered fluence. The irradiation setup is subsequently presented. Finally, the evolution of the depletion depth with fluence is described and compared with other irradiation campaigns.

4.1 The Bern medical cyclotron facility

The Bern Cyclotron facility is a partnership between the Bern University Hospital, the University of Bern and private investors. It hosts a commercial IBA18/18 medical cyclotron accelerating H^- to 18 MeV. Radioisotope production for medical usage is performed during the night, but since the facility uniquely features a 6.5 m long beam transfer line (BTL), multidisciplinary research activities can be conducted during the day [54].
As pictured in Figure 4.1, the BTL delivers the beam from the cyclotron to a second bunker. It consists of an X-Y magnet steering system, a collimator and two quadrupole doublets that allow focusing of the beam and a transmission efficiency of more than 95% [55]. More information about the BTL can be found in [56]. The 1.8 m thick wall between the bunkers together with a movable cylindrical neutron shutter stops the fast neutron flux. This neutron shielding keeps the activity in the second bunker to levels below 20 µSv/hr, allowing access few minutes after the beam is switched off, which would not be possible in the cyclotron bunker.
Even though the cyclotron was designed for high currents above 10 µA for efficient radioisotope production, currents at the pA level can be achieved by using optimised settings of the main coil, the radio-frequency system and the BTL magnets [55]. For the irradiation of the H35 samples, currents of $\sim$ 10–100 nA were used.

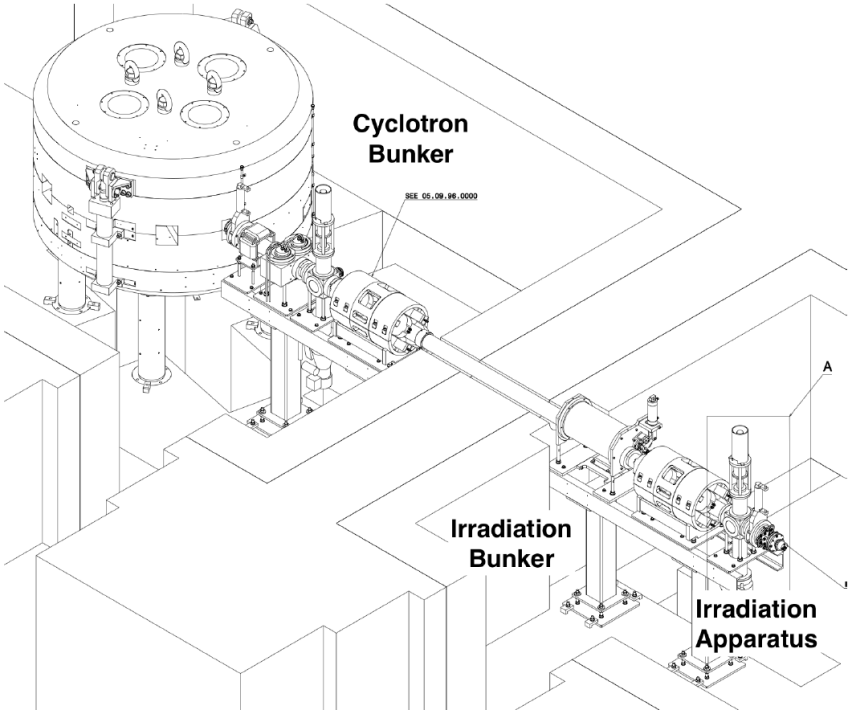

Figure 4.1: Sketch of the beam transfer line (BTL) guiding the protons from the Cyclotron to a second bunker. An X-Y magnet steering system and two quadrupole doublets allow for a transmission efficiency of $\geq 95\%$ to the irradiation setup at the end of the BTL. The thick wall and the neutron shielding keep the activity in the second bunker below $20\,\mu\text{Sv/hr}$, enabling safe access shortly after the beam is turned off.

4.2 Fluence measurement technique

As discussed in Section 2.4, radiation damage is expressed in NIEL in terms of damage 1 MeV neutrons would do. Because the cyclotron is irradiating the sensors with protons, the damage from protons has to be transferred to damage in terms of NIEL. The 1 MeV n_{eq} fluence is calculated as

$$\Phi[1\,\text{MeV n}_{\text{eq}}] = \int_0^\infty \kappa(E)\Phi(E)\text{d}E\,, \tag{4.1}$$

where $\Phi(E)$ is the fluence of the beam particles with energy E, defined as the number of particles per unit area. By knowing the energy distribution of the beam and $\kappa(E)$ of the particles (protons in this study) in the material, the fluence in 1 MeV $\text{n}_{\text{eq}}/\text{cm}^2$ can be calculated by measuring the total fluence of protons Φ. It is equal to the integrated current density of the protons $j(t)$ over the time interval $[t_0, t_1]$ of the irradiation, divided by the elementary charge

$$\Phi = \int_{t_0}^{t_1} \frac{j(t)}{e}\text{d}t\,. \tag{4.2}$$

The manner of current per unit area measurement is discussed in the following section together with the irradiation setup.

4.3 Irradiation setup

In order to measure the proton current density and ensure a flat beam profile, the irradiation setup shown in Figure 4.2 was developed. The setup is located at the end of the BTL and consists of the transverse beam profile detector Π_2, the collimator and a 2D stage to put the samples on. The collimator shapes the beam, collecting the outer part to measure the current density.

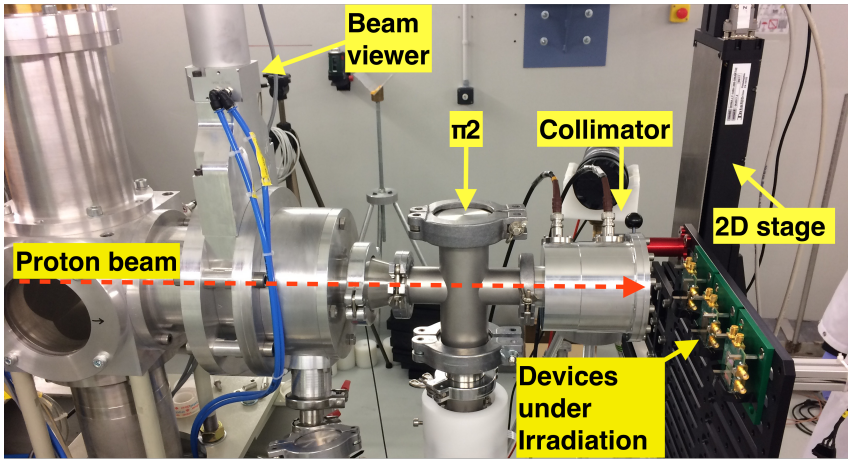

Figure 4.2: Irradiation setup at the Bern Cyclotron BTL bunker. The Π_2 detector measures the transverse beam profile and the collimator system shapes the beam and measures the current density. The beam is delivered to the DUTs which sit on a movable 2D stage.

A flat beam profile has to be ensured for the current density measurement and to irradiate the DUTs evenly. For this purpose, the novel Π_2 detector was developed at the University of Bern in [57, 58]. A thin aluminium foil is coated with the scintillation material P47 (Y_2SiO_5: Ce, Tb) and is located at an angle of 45° relative to the beam axis. Protons passing through this foil ionise, causing P47 to scintillate. The emitted light is captured by a Raspberry Pi Camera [59], which is placed orthogonally to the beam axis. As the light yield is proportional to the current density of the beam, a two-dimensional histogram of the beam profile is measured. This method of measuring the beam profile is non-destructive and leaves the beam relatively unaffected. A typical beam profile during sample irradiations is seen in Figure 4.3.
The cross section of the collimator system for the current density measurement is depicted in Figure 4.4. The beam enters from the BTL on the left through a 40 mm circular window. The beam diameter is reduced to 35 mm by a shaping ring, protecting the high voltage ring behind it. The next stage is the dump ring acting as a beam dump with a collimator window, leaving a beam of $1 \times 1\,\mathrm{cm}^2$ to be incident on the DUT. The protons

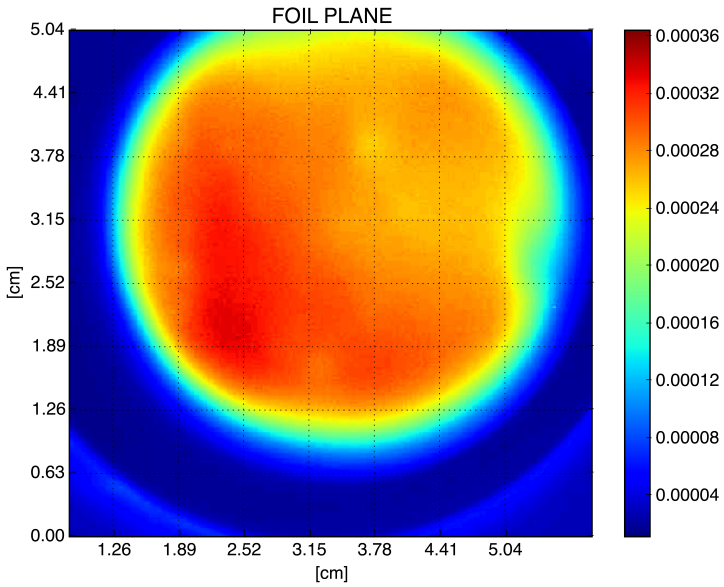

Figure 4.3: Transverse beam profile obtained with the Π_2 detector. The colour scale is in arbitrary units but is proportional to the particle flux.

impinging on the dump ring create a negative current $i(t)$ which is read out by a Keysight B2985A electrometer that has a 0.01 fA minimum current resolution [60]. Some protons kick out electrons of the dump ring. This would create a positive current, falsifying the measurement of the proton current density. Therefore, a high voltage is applied between the HV and the dump ring, pulling the electrons back onto the dump ring to negate this process.
The collimator system is under the same vacuum as the BTL with a pressure of ~ 0.01 mbar. This prohibits ionisation of air by the beam which would also affect the proton current density measurement.
Assuming a flat beam profile, the proton current density can be calculated from the measured current $i(t)$ on the dump ring by

$$j(t) = \frac{i(t)}{A_{\mathrm{BD}}} = \frac{i(t)}{\pi \cdot r_{\mathrm{shaping}} - A_{\mathrm{Coll.}}} \cdot \lambda \,, \tag{4.3}$$

where A_{BD} is the beam dump area, r_{shaping} the radius of the shaping ring, $A_{\mathrm{Coll.}}$ the collimator window area and λ is a correction factor calculated from the Π_2 beam profile. Finally, the remaining beam passes through a 300 µm aluminium extraction window needed for the vacuum and leaves the system, irradiating the device under test mounted in front of it. The protons of the beam lose energy when passing through the extraction window which changes the radiation damage delivered to the sample as $\kappa(E)$ is energy dependent. The beam energy of the Bern Cyclotron was measured in reference [61] and is displayed by the red points in Figure 4.5 together with the simulated effect of the extraction window in blue, performed with SRIM 2013 [62]. The mean energy of the

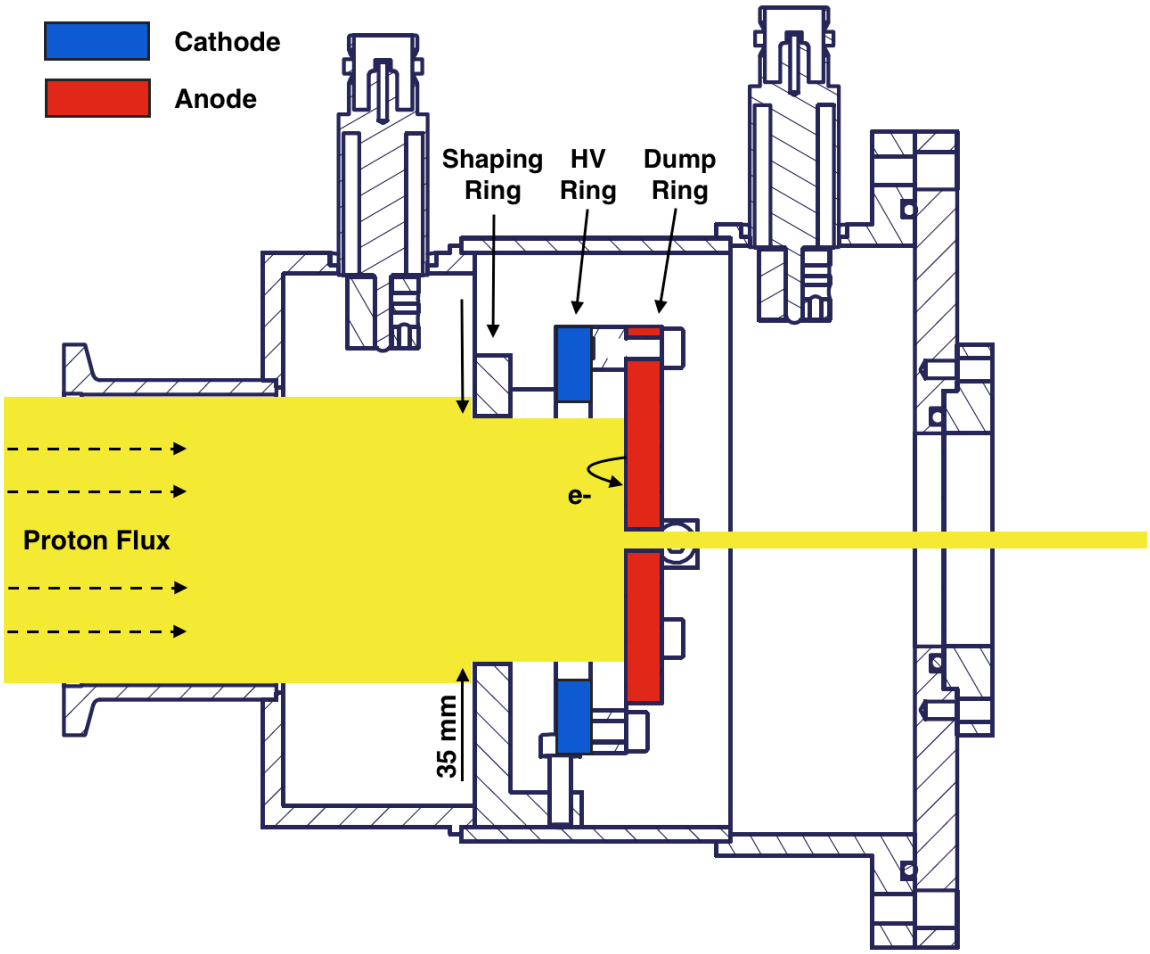

Figure 4.4: Cross section of the collimator system for measuring the proton current density. Most of the collimator system is made out of aluminium in order to keep activation at a minimum.

protons shifts down from 18.3 ± 0.4 MeV to 16.7 ± 0.5 MeV, which has to be taken as the energy for the hardness parameter $\kappa(E)$ in Equation (4.1).

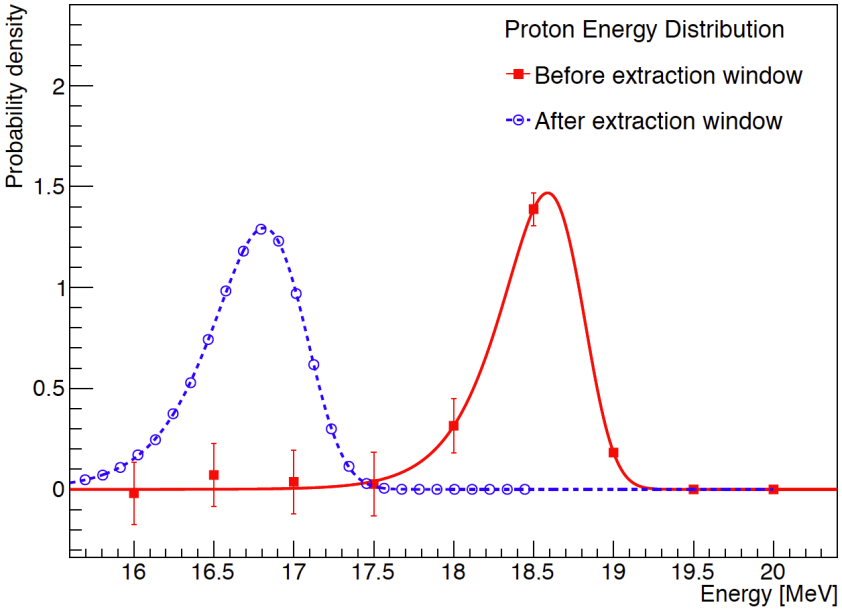

Figure 4.5: The proton energy distribution was measured in reference [61] and is displayed by red points. The fit in red was done using the Verhulst function as in reference [61]. The proton energy distribution after the 300 µm thick extraction window was simulated with SRIM 2013 [62] and is seen in blue, fitted with the Verhulst function convoluted with a Gaussian.

The last part of the irradiation setup is a stage system. It consists of a XY-BSMA-140H-300X300 2D stage from Intellidrives [63]. It features two motorised actuators with a spatial resolution of 1 µm. A mobile system to align the stage with the collimator system was developed. With this stage system, it is possible to efficiently irradiate multiple samples after each other without entering the bunker.

4.4 Verification of delivered fluence

The fluence measurements with the collimator system described in the previous sections are verified by radiochromic films. The films change their optical absorbance linearly with ionising dose. The films used are FWT-60 produced by Far West Technology (FWT) and are made of 47 ± 5 µm hexa(hydroxyethyl) aminotriphenylacetonitrile (HHEVC) dyes [64]. As a calibration, the films were put in front of the beam and irradiated to different doses as measured with the collimator system.
After the irradiation, the optical absorbance of the films is measured at a specific wavelength using a spectrometer following the prescription of FWT. The comparison between the dose of the collimator system and the manufacturer calibration is seen in Figure 4.6. The vertical error bar assumes an error of 1 µm on the thickness of the film, while the

error on the dose comes from the uncertainty on the energy loss calculation in HHEVC by SRIM ($30.87 \pm 5\%$ MeV cm^2/g) and from the current measurement. The measurements at the Bern Cyclotron are consistent with the FWT calibration within uncertainties, verifying the fluence measurement technique.

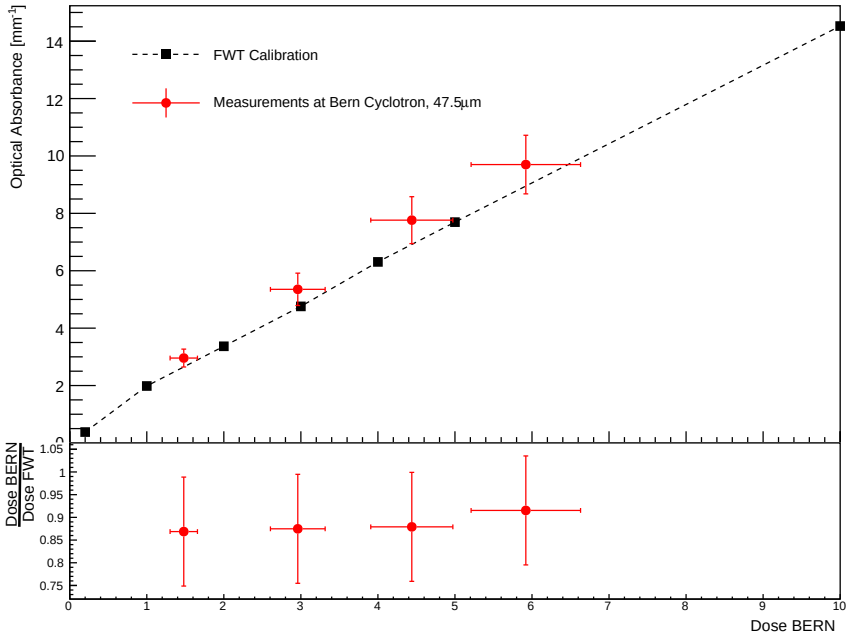

Figure 4.6: The calibration of the radiochromic films performed by Far West Technology compared with the measurements done at the Bern Cyclotron. For the latter, the dose measurement was performed with the collimator system described in Section 4.3.

4.5 Characterisation of irradiated samples

H35 demonstrator chip of all resistivities were irradiated to 1 MeV neutron equivalent fluences of up to $\sim 1.5 \cdot 10^{15}$/cm^2 with 16.7 MeV protons, together with their PCB's. The irradiations were normally conducted every week, characterising the samples in between the irradiations. In this time, the chips have been stored at room temperature.
Figure 4.7 displays how the depletion depth versus bias voltage curves evolve with NIEL. The curves are fitted in the same way as before irradiation (with Equation (2.4)), but not limiting the built-in voltage. The depletion depth of the 20 Ω cm sample does not change for small fluences, but increases heavily at the $8 \cdot 10^{14}$ 1 MeV n$_{eq}$/cm^2 point. For the other resistivities, the depletion depth increases for low fluences, but goes down again for high ones. The lower resistivity chips have a depletion depth at the highest fluence that is larger than before irradiation; their performance improves after irradiation. In contrast to this, it is smaller for the high resistivity chip of 1000 Ω cm. Its depletion region at

−100 V bias voltage is ∼ 140 µm deep before irradiation, but shrinks to ∼ 125 µm after the total fluence.

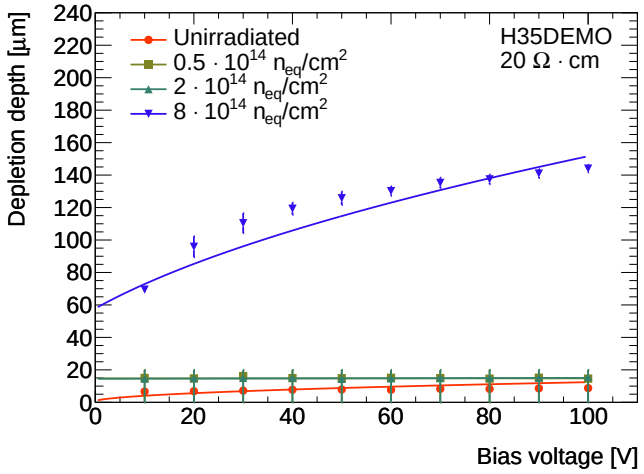

(a) 20 Ω cm sample

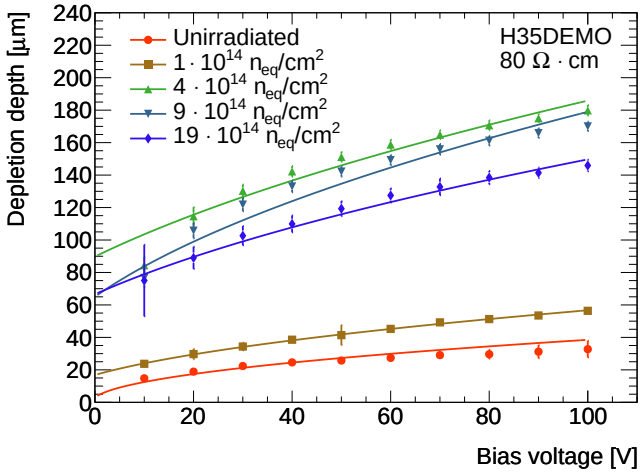

(b) 80 Ω cm sample

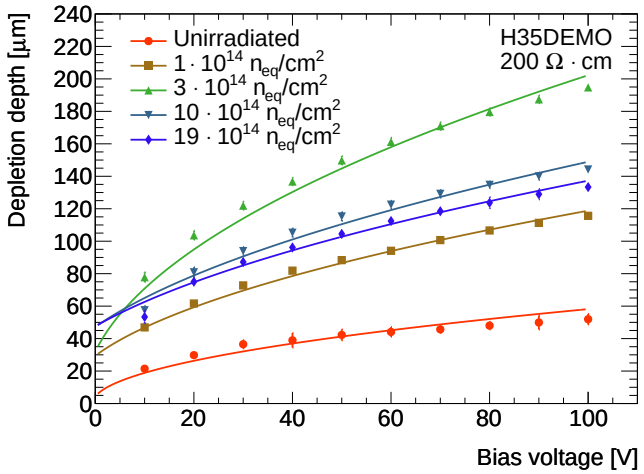

(c) 200 Ω cm sample

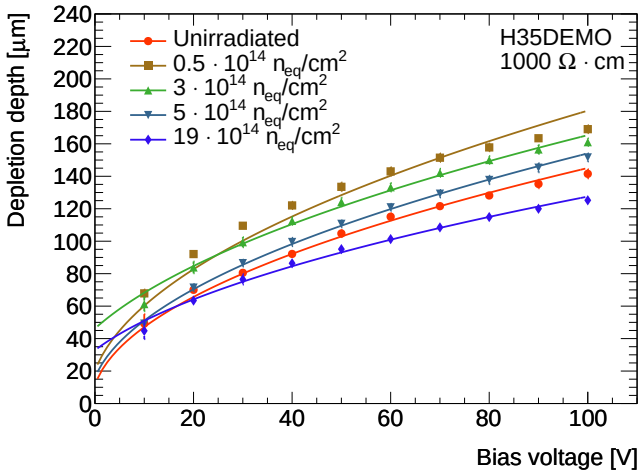

(d) 1000 Ω cm sample

Figure 4.7: Depletion depth versus bias voltage for selected fluences delivered by the Bern Cyclotron 16.7 MeV protons.

In order to see the evolution of the depletion depth with fluence more clearly, Figure 4.8 shows the depletion depth for a fixed bias voltage of −80 V for all resistivities. The error bars on the fluence originate from the uncertainty on the current density measurement. It can be clearly seen that the depletion depth first increases and then at a NIEL of $2\text{–}3 \cdot 10^{14}$ 1 MeV n_{eq}/cm^2 (tipping point) decreases again for ρ of 80, 200 and 1000 Ω cm. The tipping point can not be precisely localised for the 20 Ω cm sample since there are not many irradiation points. An evolution of this kind can be explained by the acceptor removal effect mentioned in Section 2.4. It yields an effective decrease of acceptor con-

centration thus increasing the depletion depth (for $N_D \gg N_A$). For high enough NIEL, trapping dominates over the acceptor removal and leads to a smaller collection efficiency, reducing the depletion depth again [39].

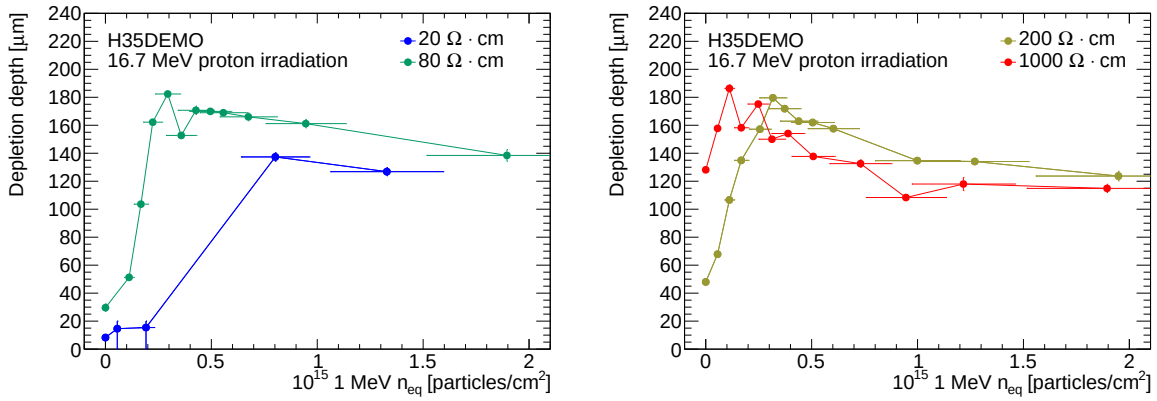

(a) 20 and 80 Ω cm samples

(b) 200 and 1000 Ω cm samples

Figure 4.8: Evolution of depletion depth of the H35 demonstrator chip with NIEL after 16.7 MeV proton irradiation at a bias voltage of −80 V.

Another interesting feature seen in Figure 4.8 are the dips in the evolution of the depletion depth observed in the 80 (at $\sim 3 \cdot 10^{14}$ 1 MeV n_{eq}/cm^2) and 1000 Ω cm samples (at $\sim 2.2 \cdot 10^{14}$ 1 MeV n_{eq}/cm^2). In the latter this could be explained by the large time span in between the second and third irradiation of the sample. Since the samples were stored at room temperature, the 1000 Ω cm sample could anneal, reverting part of the acceptor removal effect. This would lead to the observed lower depletion depth after a long annealing time.

4.6 Comparison with other irradiations campaigns

The H35 demonstrator chip was also irradiated with 24 GeV p^+ at the Proton Synchrotron (PS) at CERN and characterised as the Bern Cyclotron irradiated H35 samples. Figure 4.9 shows the evolution of the depletion depth versus bias voltage curves with fluence after this irradiation.
A characterisation of 80, 200 and 1000 Ω cm resistivities of the H35 demonstrator chip was performed in [15], irradiating with 1 MeV neutrons instead of protons. No neutron irradiation data is available for 20 Ω cm. The results of the two proton at PS and the Bern Cyclotron are compared with this neutron irradiation in Figure 4.10 for a fixed bias voltage of −80 V. The evolution of the depletion depth is similar for the two proton irradiations. They both feature an increase that could be explained by the acceptor removal phenomenon as discussed in the previous section. Looking more closely at the results from the PS irradiation, it is seen that at high fluences the depletion depth falls off slightly more rapidly for the 80, 200 and 1000 Ω cm samples than in the Bern Cyclotron

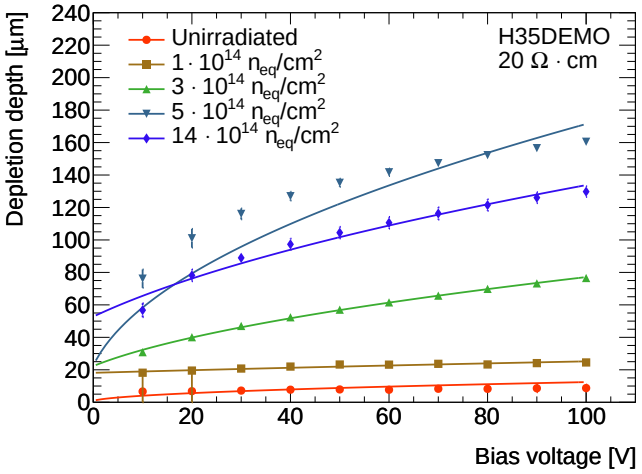

(a) 20 Ω cm sample

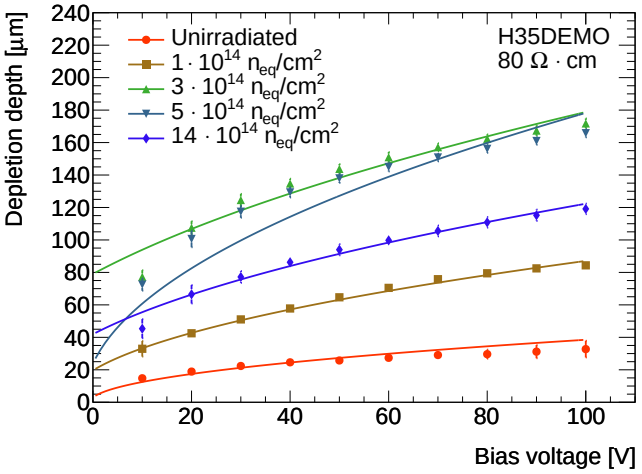

(b) 80 Ω cm sample

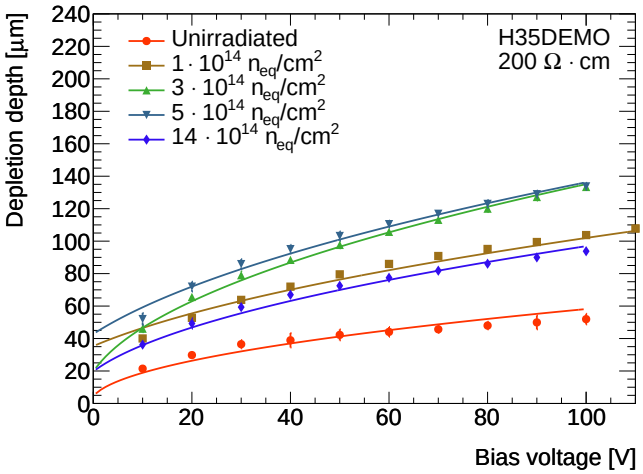

(c) 200 Ω cm sample

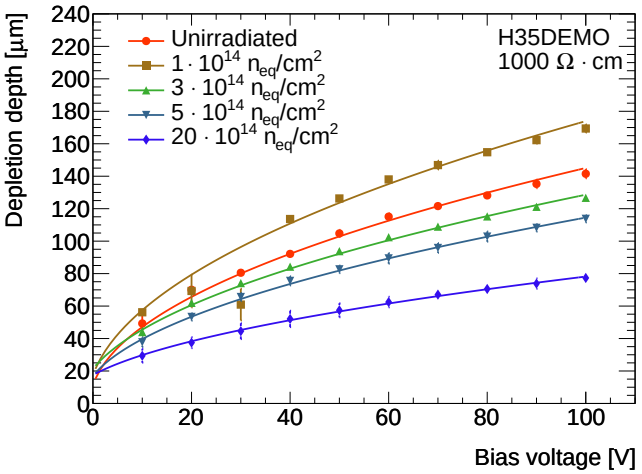

(d) 1000 Ω cm sample

Figure 4.9: Depletion depth versus bias voltage for selected fluences delivered by the CERN PS 24 GeV protons.

irradiation. Furthermore, the PS irradiated 200 and 1000 Ω cm sample does not reach as large depletion depths as the Bern Cyclotron irradiated sample. A possible explanation is that the acceptor removal process happens more slowly for 24 GeV protons. Hence, trapping keeps the depletion depth small at low fluences. The results on the 200 Ω cm sample supports this argument by having a tipping point in the 24 GeV irradiation at $\sim 0.6 \cdot 10^{15}$ 1 MeV n_{eq}/cm^2, which is at much higher fluence than in the Bern Cyclotron irradiated case at $\sim 0.3 \cdot 10^{15}$ 1 MeV n_{eq}/cm^2. For a detailed analysis of the 20 Ω cm sample, more irradiation points are needed, especially in order to determine the position of the tipping point.
Looking at the results from neutron irradiation, it is seen that the depletion depth is increasing with fluence for 80 and 200 Ω cm, but by a far smaller extent than in the proton case. The 80 Ω cm sample for example only features a maximal depletion depth of ~ 60 µm at $1 \cdot 10^{15}$ 1 MeV n_{eq}/cm^2, while it goes up to more than 180 µm in the 16.7 MeV proton irradiation. The tipping points of these resistivities are also at higher fluences than in the proton irradiations, but given the small number of irradiation points, a good estimation is difficult to achieve. The 1000 Ω cm sample paints a very different picture. The depletion depth is only decreasing with radiation for neutrons, while an increase was observed in the proton irradiation for fluences up to $\sim 0.2 \cdot 10^{15}$ 1 MeV n_{eq}/cm^2.
Following the above discussion it can be concluded that the acceptor removal effect, which is responsible for the increase of depletion depth, also happens in irradiation with protons. The results of the two proton energies of 16.7 MeV and 24 GeV show small differences. 16.7 MeV irradiated samples have slightly higher depletion depths. In neutron irradiations, the acceptor removal effect is even weaker and is barely increasing the depletion depth in comparison to the proton irradiations.

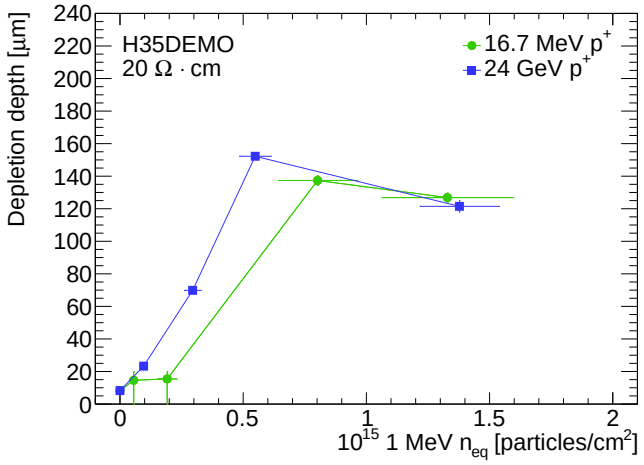

(a) 20 Ω cm sample

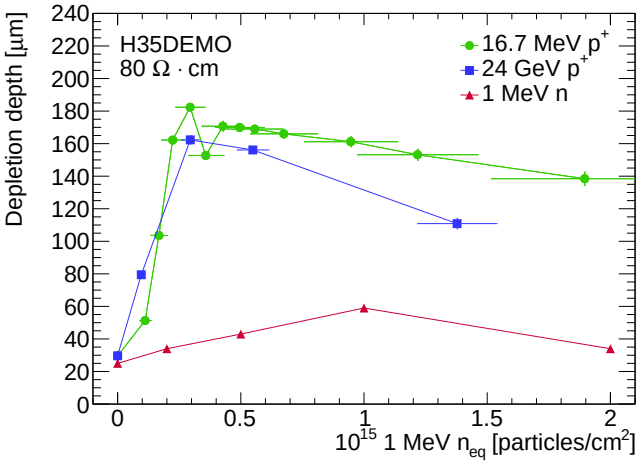

(b) 80 Ω cm sample

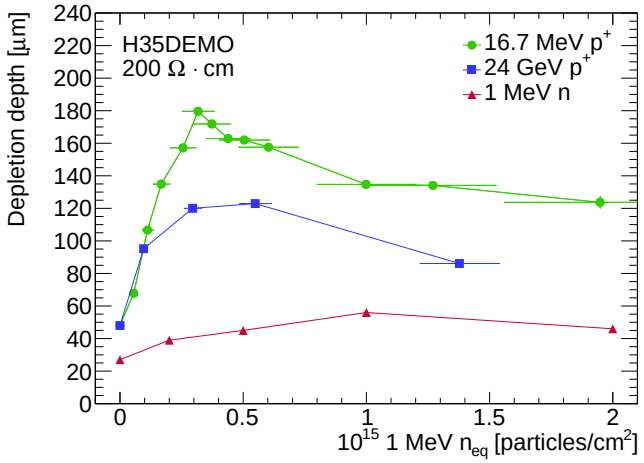

(c) 200 Ω cm sample

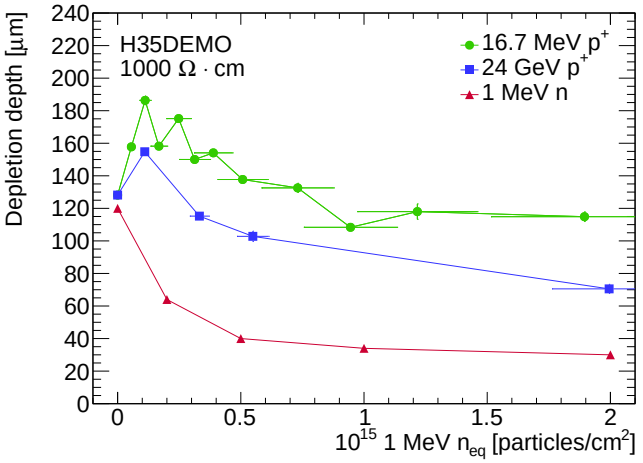

(d) 1000 Ω cm sample

Figure 4.10: Depletion depth evolution with radiation damage from three different incident particles at −80 V bias voltage. The neutron data is taken from [15].

Conclusions

In this thesis I presented a characterisation of the H35 demonstrator chip produced in the HV-CMOS technology. The depletion region of samples of different resistivities was measured before and after irradiation with the Transient Current Technique. I was involved in setting up and validating the TCT setup and I developed a dedicated analysis to calculate the depletion depth. The chips were irradiated with protons of two different energies to fluences of up to $\sim 1.5 \cdot 10^{15}$ 1 MeV n_{eq}/cm^2, which is the expected fluence for the fifth pixel layer of the ITk. I was heavily involved in the irradiation campaign at the Bern Cyclotron, for which an irradiation setup measuring the delivered fluence was developed, making the Bern Cyclotron a very capable facility for radiation hardness studies. I constructed the stage system and was involved in the development of the collimator system. I presented the developments at the Bern Cyclotron facility at the Joint Annual Meeting of the Swiss and Austrian Physical Society [65] and a paper will be published soon as well. The results of the TCT characterisation were presented by me in the Trento Workshop on Advanced Silicon Radiation Detectors [66] and are soon to be published in a paper.

The depletion depth evolution of the two proton irradiation campaigns was compared with a study performed with 1 MeV neutrons [15]. The acceptor removal seen in the neutron irradiation was also observed with protons, but to a much larger extent. Depletion depths after proton irradiation are generally greater than 100 µm while being less than 50 µm after neutron irradiation at a bias voltage of −80 V. The energy of the protons was observed to also play a role since the depletion depths measured in the Bern Cyclotron irradiated samples are bigger than samples inflicted with 24 GeV protons from the Proton Synchrotron at CERN. The 80 and 200 Ω cm resistivities feature a high depletion depth up to tested fluences of more than $1.5 \cdot 10^{15}$ 1 MeV n_{eq}/cm^2 for all different irradiations. The 20 Ω cm sample has a depletion depth of less than 20 µm before irradiation, due to which it is considered an inferior option. In contrast to the other resistivity samples, the 1000 Ω cm sample starts with high depletion depths of $\sim$ 130 µm at −80 V bias voltage, but falls lower than the 80 and 200 Ω cm samples for high fluences. This study suggests that sensors produced in the ams HV-CMOS process would be radiation tolerant enough to be a viable option for the fifth layer of the ATLAS ITk, depending on the sensor's resistivity. However, other properties also have to be taken into account for a final decision on the most suitable sensor candidate.

In future studies, the sensors should be stored below −20 °C. Since this stops annealing, the depletion depth should stay constant in between irradiations. The installation of a

storing system capable of cooling the sensors to $-40\,°C$ is currently under way at the Bern Cyclotron. Furthermore, the current study could be expanded by adding more irradiation steps to the $20\,\Omega\,cm$ sample, giving a more complete picture of the depletion depth evolution.
The next generation of ams AG HV-CMOS monolithic chips is produced in a 180 nm process [67]. The corresponding H18 demonstrator chip is scheduled to be studied in a test beam, investigating other properties of the sensors. Furthermore, it would be of interest to perform irradiations with multiple types of particles on the same samples, since the sensors used in the ITk will not only receive damage from one type of particle but from a mixture. Do the damages add up linearly or are new effects observed? A further study would be to investigate photon irradiations that allow to inflict only ionising damage to the sensors.

Bibliography

[1] ATLAS Collaboration. Observation of a new particle in the search for the standard model higgs boson with the ATLAS detector at the LHC. *Physics Letters B*, 716(1):1–29, September 2012. doi:10.1016/j.physletb.2012.08.020. 5

[2] Werner Herr and B Muratori. Concept of luminosity. Available at https://cds.cern.ch/record/941318 accessed 18.02.2018, 2006. 7

[3] Geneva CERN. Cern yellow reports, vol 4 (2016): Updated baseline for a staged compact linear collider. 2016. doi:10.5170/cern-2016-004. 7

[4] Lyndon Evans and Philip Bryant. LHC machine. *Journal of Instrumentation*, 3(08):S08001–S08001, August 2008. doi:10.1088/1748-0221/3/08/s08001. 8

[5] M. Solfaroli. Review of 2017 operation, January 2018. LHC performance workshop, Chamonix 2018. Available at https://indico.cern.ch/event/676124/contributions/2767793/ accessed 22.02.2018. 8

[6] S. Myers and E. Picasso. The design, construction and commissioning of the CERN large electron–positron collider. *Contemporary Physics*, 31(6):387–403, November 1990. doi:10.1080/00107519008213789. 8

[7] Robert R. Wilson. The Tevatron. *Physics Today*, 30(10):23–30, October 1977. doi:10.1063/1.3037746. 8

[8] Esma Anais Mobs. The CERN accelerator complex. Complexe des accélérateurs du CERN, October 2016. Available at https://cds.cern.ch/record/2225847 accessed 21.02.2018. 9

[9] The ATLAS Collaboration. The ATLAS experiment at the CERN Large Hadron Collider. *Journal of Instrumentation*, 3(08):S08003–S08003, August 2008. doi:10.1088/1748-0221/3/08/s08003. 10

[10] Joao Pequenao. Computer generated image of the whole ATLAS detector, March 2008. Available at https://cds.cern.ch/record/1095924 accessed 21.02.2018. 11

[11] M Capeans, G Darbo, K Einsweiller, M Elsing, T Flick, M Garcia-Sciveres, C Gemme, H Pernegger, O Rohne, and R Vuillermet. ATLAS Insertable B-Layer

Technical Design Report. Technical Report CERN-LHCC-2010-013. ATLAS-TDR-19, ATLAS Collaboration, September 2010. URL: https://cds.cern.ch/record/1291633. 10, 25

[12] ATLAS Collaboration. ATLAS Phase-II Upgrade Scoping Document. Technical Report CERN-LHCC-2015-020. LHCC-G-166, CERN, Geneva, September 2015. URL: http://cds.cern.ch/record/2055248. 12

[13] ATLAS Collaboration. Technical Design Report for the ATLAS Inner Tracker Pixel Detector. Technical Report CERN-LHCC-2017-021. ATLAS-TDR-030, CERN, Geneva, September 2017. URL: http://cds.cern.ch/record/2285585. 12, 13, 14, 26

[14] ATLAS Collaboration. Technical Design Report for the ATLAS Inner Tracker Strip Detector. Technical Report CERN-LHCC-2017-005. ATLAS-TDR-025, CERN, Geneva, April 2017. URL: http://cds.cern.ch/record/2257755. 12

[15] E. Cavallaro, R. Casanova, F. Förster, S. Grinstein, J. Lange, G. Kramberger, I. Mandić, C. Puigdengoles, and S. Terzo. Studies of irradiated AMS h35 CMOS detectors for the ATLAS tracker upgrade. *Journal of Instrumentation*, 12(01):C01074–C01074, January 2017. doi:10.1088/1748-0221/12/01/c01074. 13, 26, 34, 49, 52, 53

[16] A Fassò, A Ferrari, Johannes Ranft, and Paola R Sala. Fluka: A multi-particle transport code (program version 2005), 2005. doi:10.5170/cern-2005-010. 14

[17] Torbjörn Sjöstrand, Stephen Mrenna, and Peter Skands. A brief introduction to PYTHIA 8.1. *Computer Physics Communications*, 178(11):852–867, June 2008. doi:10.1016/j.cpc.2008.01.036. 14

[18] H. Bethe. Zur Theorie des Durchgangs schneller Korpuskularstrahlen durch Materie. *Annalen der Physik*, 397(3):325–400, 1930. doi:10.1002/andp.19303970303. 15

[19] F. Bloch. Zur bremsung rasch bewegter teilchen beim durchgang durch materie. *Annalen der Physik*, 408(3):285–320, 1933. doi:10.1002/andp.19334080303. 15

[20] Antonio Miucci, Giuseppe Iacobucci, Alessandro La Rosa, and Didier Ferrere. *The construction of the Insertable B-Layer and the b-tagging performance at high-p_T of the ATLAS experiment*. PhD thesis, January 2016. Presented 24 February 2016. URL: https://cds.cern.ch/record/2237669. 15, 16, 18, 23

[21] K.A. Olive. Review of particle physics. *Chinese Physics C*, 38(9):090001, August 2014. doi:10.1088/1674-1137/38/9/090001. 16

[22] Lev Davidovich Landau. On the energy loss of fast particles by ionization. *J. Phys.*, 8:201–205, 1944. 16

[23] PV Vavilov. Ionization losses of high-energy heavy particles. *Soviet Phys. JETP*, 5, 1957. 16

[24] K.A. Olive. Review of particle physics. *Chinese Physics C*, 40(10):100001, October 2016. doi:10.1088/1674-1137/40/10/100001. 17, 20

[25] Leonardo Rossi, Peter Fischer, Tilman Rohe, and Norbert Wermes. *Pixel detectors: From fundamentals to applications*. Springer Science & Business Media, 2006. doi:10.1007/3-540-28333-1. 17, 19, 20

[26] Igor Kreslo. Lecture notes in Measurement Techniques. University of Bern, October 2016. 17

[27] Francis Berghmans, Benoît Brichard, Alberto Fernandez Fernandez, Andrei Gusarov, Marco Van Uffelen, and Sylvain Girard. An introduction to radiation effects on optical components and fiber optic sensors. In *Optical Waveguide Sensing and Imaging*, pages 127–165. Springer Netherlands. doi:10.1007/978-1-4020-6952-9_6. 18

[28] Gerhard Lutz. *Semiconductor Radiation Detectors*. Springer Berlin Heidelberg, 2007. doi:10.1007/978-3-540-71679-2. 18, 19, 20, 22, 23, 24

[29] Niraj Chawake. Semiconductors: Why $\Delta E \leq 3.2$ eV? Available at https://nirajchawake.wordpress.com/2014/10/20/ accessed 05.01.2018, 2014. 19

[30] User TheNoise at the English language Wikipedia. A PN junction in thermal equilibrium with zero bias voltage applied. Available at https://commons.wikimedia.org/wiki/File:Pn-junction-equilibrium-graphs.png accessed 28.12.2017. 21, 22

[31] Martin J Berger, JS Coursey, MA Zucker, and J Chang. *Stopping-power and range tables for electrons, protons, and helium ions*. NIST Physics Laboratory Gaithersburg, MD, 1998. 20

[32] U. Fano. Ionization yield of radiations. II. the fluctuations of the number of ions. *Physical Review*, 72(1):26–29, July 1947. doi:10.1103/physrev.72.26. 22

[33] S M Sze. *Semiconductor devices: physics and technology; 2nd ed.* Wiley, New York, NY, 2002. URL: http://cds.cern.ch/record/559335. 22

[34] Michael Moll. *Radiation damage in silicon particle detectors: Microscopic defects and macroscopic properties*. PhD thesis, 1999. 23, 24

[35] Victor AJ Van Lint, TM Flanagan, RE Leadon, James A Naber, and VC Rogers. Mechanisms of radiation effects in electronic materials. volume 1. *NASA STI/Recon Technical Report A*, 81, 1980. 23

[36] Gunnar Lindström. Radiation damage in silicon detectors. *Nuclear Instruments and Methods in Physics Research Section A: Accelerators, Spectrometers, Detectors and Associated Equipment*, 512(1-2):30–43, October 2003. doi:10.1016/s0168-9002(03)01874-6. 24, 25

[37] Vladimir Cindro, Gregor Kramberger, Manuel Lozano, Igor Mandić, Marko Mikuž, Giulio Pellegrini, Jožef Pulko, Miguel Ullan, and Marko Zavrtanik. Radiation damage in p-type silicon irradiated with neutrons and protons. *Nuclear Instruments and Methods in Physics Research Section A: Accelerators, Spectrometers, Detectors and Associated Equipment*, 599(1):60–65, February 2009. doi:10.1016/j.nima.2008.11.007. 24

[38] Collaboration ATLAS. Inner detector technical design report. Technical report, 1997. URL: https://cds.cern.ch/record/331063. 25

[39] Branislav Ristic. Active pixel sensors in AMS H18/H35 HV-CMOS technology for the ATLAS HL-LHC upgrade. *Nuclear Instruments and Methods in Physics Research Section A: Accelerators, Spectrometers, Detectors and Associated Equipment*, 831:88–93, September 2016. doi:10.1016/j.nima.2016.06.001. 25, 26, 49

[40] E. Vilella, M. Benoit, R. Casanova, G. Casse, D. Ferrere, G. Iacobucci, I. Peric, and J. Vossebeld. Prototyping of an HV-CMOS demonstrator for the high luminosity-LHC upgrade. *Journal of Instrumentation*, 11(01):C01012–C01012, January 2016. doi:10.1088/1748-0221/11/01/c01012. 26, 27

[41] 350 nm HV-CMOS process of ams AG. Available at http://ams.com/eng/Products/Full-Service-Foundry/Process-Technology/High-Voltage-CMOS/0.35-m-HV-CMOS-process accessed 17.02.2018. 26

[42] M. Benoit et al. Test beam measurement of ams H35 HV-CMOS capacitively coupled pixel sensor prototypes with high-resistivity substrate. 2017. arXiv:1712.08338. 26

[43] G. Kramberger, V. Cindro, I. Mandic, M. Mikuz, M. Milovanovic, M. Zavrtanik, and K. Zagar. Investigation of irradiated silicon detectors by edge-TCT. *IEEE Transactions on Nuclear Science*, 57(4):2294–2302, August 2010. doi:10.1109/tns.2010.2051957. 28

[44] Gregor Kramberger. Advanced Transient Current Technique Systems. *PoS*, Vertex2014:032, 2015. 29, 33

[45] Scanning-TCT setup from Particulars. Available at http://www.particulars.si/products.php?prod=scanTCT.html accessed 25.01.2018. 29

[46] Specifications of LA-01 IR FC laser from Particulars. Available at http://www.particulars.si/products.php?prod=lasers.html accessed 25.01.2018. 29

[47] Spec sheet of Keithley 2410 source meter. Available at http://download.tek.com/datasheet/2400_SMU_Datasheet_1KW-2798-1.pdf accessed 03.02.2018. 30

[48] Specsheet of AM-02 charge-sensitive amplifier from Particulars. Available at http://particulars.si/downloads/ParticularsAmps-Manuals.pdf accessed 16.01.2018. 30

[49] Paul Scherrer Institut (PSI). Available at https://www.psi.ch/drs/evaluation-board accessed 22.12.2017. 30

[50] Specification sheet of laser power sensor OP-2 VIS from Coherent. Available at https://edge.coherent.com/assets/pdf/High-Sensitivity-Optical-Power-Sensors.pdf accessed 25.12.2017. 31

[51] George B Arfken, Hans J Weber, and Frank E Harris. *Mathematical Methods For Physicist A Comprehensive Guide*, volume 20. 2013. 31, 35

[52] Rene Brun and Fons Rademakers. ROOT — an object oriented data analysis framework. *Nuclear Instruments and Methods in Physics Research Section A: Accelerators, Spectrometers, Detectors and Associated Equipment*, 389(1-2):81–86, April 1997. doi:10.1016/s0168-9002(97)00048-x. 32

[53] Particulars, Advanced measurement systems, Ltd.. Available at http://particulars.si accessed 21.12.2017. 32

[54] Saverio Braccini, A Ereditato, Paola Scampoli, and Konrade von Bremen. The new Bern cyclotron laboratory for radioisotope production and research. In *Proceedings of the Second International Particle Accelerator Conference–IPAC2011 (3618). San Sebastian, Spain*, 2011. 41

[55] M Auger, S Braccini, A Ereditato, K P Nesteruk, and P Scampoli. Low current performance of the bern medical cyclotron down to the pA range. *Measurement Science and Technology*, 26(9):094006, July 2015. doi:10.1088/0957-0233/26/9/094006. 41

[56] Saverio Braccini. The new Bern PET cyclotron, its research beam line, and the development of an innovative beam monitor detector. In *AIP Conference Proceedings*, volume 1525, pages 144–150. AIP, 2013. 41

[57] Meinrad Schefer. Study of a novel two-dimensional online beam monitoring detector. Bachelor thesis, University of Bern, February 2018. Supervisor: Saverio Braccini. 43

[58] Matthias Schmid. Development and optimization of a two-dimensional beam monitoring detector at the bern medical cyclotron laboratory. Bachelor thesis, University of Bern, February 2018. Supervisor: Saverio Braccini. 43

[59] Raspberry Pi Camera Module v2. Available at https://www.raspberrypi.org/products/camera-module-v2/ accessed 03.02.2018. 43

[60] Keysight Technologies. B2980A Series Femto/Picoammeter and Electrometer/High Resistance Meter Data Sheet. Available at https://literature.cdn.keysight.com/litweb/pdf/5991-4878EN.pdf?id=2500920 accessed 16.01.2018. 44

[61] K.P. Nesteruk, M. Auger, S. Braccini, T.S. Carzaniga, A. Ereditato, and P. Scampoli. A system for online beam emittance measurements and proton beam characterization. *Journal of Instrumentation*, 13(01):P01011–P01011, January 2018. doi:10.1088/1748-0221/13/01/p01011. 44, 46

[62] James F. Ziegler, M.D. Ziegler, and J.P. Biersack. SRIM – the stopping and range of ions in matter (2010). *Nuclear Instruments and Methods in Physics Research Section B: Beam Interactions with Materials and Atoms*, 268(11-12):1818–1823, June 2010. doi:10.1016/j.nimb.2010.02.091. 44, 46

[63] Specifications of 2D movable stage used at the irradiation setup. Available at http://www.intellidrives.com/XY-tables-XYZ-Systems/XY-Tables/XY-Table-BSMA-LY-140H-300x300 accessed 03.02.2018. 46

[64] Far West Technology. FWT-60-00 radiochromic film characterisation. Available at http://www.fwt.com/racm/support/Batch1062.pdf accessed 16.01.2018. 46

[65] Armin Fehr. The Bern Cyclotron proton irradiation facility, August 2017. Talk at the Joint Annual Meeting of the Swiss Physical Society and Austrian Physical Society. Available at https://indico.cern.ch/event/611331/contributions/2645669/. 53

[66] Armin Fehr. Radiation hardness study of HV-CMOS sensors using Transient Current Technique, February 2018. Talk at 13th "Trento" Workshop on Advanced Silicon Radiation Detectors. Available at https://indico.cern.ch/event/666427/contributions/2882586/. 53

[67] 180 nm HV-CMOS process of ams AG. Available at http://ams.com/eng/Products/Full-Service-Foundry/Process-Technology/High-Voltage-CMOS/0.18-m-HV-CMOS-process accessed 18.02.2018. 54

Declaration of consent

on the basis of Article 28 para. 2 of the RSL05 phil.-nat.

Name/First Name: Fehr, Armin

Matriculation Number: 12-119-087

Study program: Master of Science in Physics, Experimental Physics

Bachelor ☐ Master ☑ Dissertation ☐

Title of the thesis: Characterisation of HV-CMOS silicon pixel sensors with a transient current technique before and after proton irradiation

Supervisor: Prof. Dr. Michele Weber

I declare herewith that this thesis is my own work and that I have not used any sources other than those stated. I have indicated the adoption of quotations as well as thoughts taken from other authors as such in the thesis. I am aware that the Senate pursuant to Article 36 para. 1 lit. r of the University Act of 5 September, 1996 is authorised to revoke the title awarded on the basis of this thesis. I allow herewith inspection in this thesis.

Bern, 03.03.2018

Place/Date

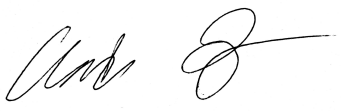

Signature